2008

# Fully coupled fluid-structure interaction model of active eustachian tube function in healthy and cleft palate patients

Francis J. Sheer
*Lehigh University*

Sheer, Francis J.

# Fully Coupled Fluid-Structure Interaction Model of Active Eustachian Tube Function in Healthy and Cleft Palate Patients

September 2008

# Fully Coupled Fluid-Structure Interaction Model of Active Eustachian Tube Function in Healthy and Cleft Palate Patients

by

Francis J. Sheer

A Thesis
Presented to the Graduate and Research Committee
of Lehigh University
in Candidacy for the Degree of
Master of Science

in

Mechanical Engineering and Mechanics

Lehigh University
August, 2008

CERTIFICATE OF APPROVAL

This thesis is accepted and approved in partial fulfillment of the requirements for the Master of Science.

8/06/2008

Date

Thesis Advisor (Samir N. Ghadiali, PhD)

Chairperson of Department (Gary Harlow, PhD)

## Acknowledgements

I would first and foremost like to thank my research advisor Dr. Samir Ghadiali for providing me with the much needed guidance to complete my Master's Thesis. His knowledge in modeling, finite element analysis, and extensive knowledge in the bioengineering field has definitely improved my research skills and prepares me for any engineering challenges I might face in the future.

I would also like to thank my other graduate students in my lab, Hannah Dailey and Xiaodong Chen, for offering their assistance when I had questions. Lastly, I would thank my parents, Steve and Teresa. Without them I would not have the wonderful opportunity to study at Lehigh University.

## Table of Contents

## List of Tables and Figures

## Nomenclature

ET- Eustachian tube
OM- Otitis Media
NP- Nasopharynx
CP- Cleft palate
ME- Middle ear
TVPM- Tensor veli palatini muscle
LVPM- Levator veli palatini muscle
FEA- Finite element analysis
CFD- Computational Fluid Dynamics
$F_{TVP}$- Total force applied by the TVPM
$F_{LVP}$- Total force applied by the LVPM
$E_{gland}$- Young's modulus of the glandular tissue
$E_{cart}$- Young's modulus of the cartilage
$\sigma^S$ – Cauchy stress tensor
W- Strain energy density
$\varepsilon$– Tissue strain
$d_i$ – Displacement of each mesh node
$\rho$ – Fluid density
$\mu$- Fluid viscosity
$\upsilon_i$ – Velocity vector
$x_i$ – Position vector
t- Time
p- Fluid pressure
$n_i$ – Interface normal vector
Q- Flow rate of air in lumen
$R_v$- Flow resistance parameter
$\Delta P$ - Pressure drop from the ME to the NP
$\upsilon_{cart}$ – Poisson's ratio of the cartilage
$\upsilon_{gland}$ –Poisson's ratio of the glandular tissue
G- Shear modulus
$\kappa$ – Bulk modulus
$J_1$ and $J_3$- Reduced strain invariants
$C_1$-$C_9$ & $D_1$, $D_2$- Material properties
DOF - Degree of Freedom
ALE - Arbitrary Lagrangian Eulerian

## Abstract

Otitis Media (OM) is the most commonly diagnosed childhood illness that affects thousands of children per year [1]. Dysfunction of the Eustachian Tube (ET), which is a collapsible tube that connects the Middle Ear (ME) to the Nasopharynx (NP), is the primary etiology of OM. In healthy adults, periodic openings of the ET due to contraction of the tensor veli palatini (TVPM) and levator veli palatini (LVPM) muscles, equalize ME pressure and/or drain ME fluid [2]. However, patients with cleft palate syndrome have a 100% incidence rate of OM due to ET dysfunction. The overall goal of this study is to develop fluid-structure interaction computational models of ET function in both healthy adult and cleft palate subjects and compare model results to identify the mechanisms responsible for dysfunction in cleft palates.

The effects of tissue morphology were investigated by creating decoupled finite element models (FEM) of both healthy adult and cleft palate ETs. Results indicate that ET function in healthy adults is highly sensitive to TVPM forces. However, in cleft patients, ET function was relatively insensitive to TVPM and LVPM forces. We conclude that the altered tissue morphology in cleft palates plays a vital role in ET dysfunction.

Experimental data suggests a strong coupling between the amount of muscle force generated and the amount of flow through the lumen. We developed coupled fluid-structure interaction (FSI) models to simulate dynamic flow phenomena during ET opening in one healthy adult and one cleft palate patient. Results indicate that although ET opening phenomena was very sensitive to the relative timings of muscle contractions in the adult subject, the cleft palate patient showed very little sensitivity to muscle timing.

We conclude that changing muscle timing is not a viable option for treating ET dysfunction in cleft palate patients.

Finally, the ET is a very complex system and several efforts were made to model more components of the system including the auditory canal, tympanic membrane and ME to better replicate experimental results. Also, new FEM techniques are being developed that can handle the large deformations experienced during ET opening and closing better than the previous models.

**Keywords**

Eustachian Tube, Otitis Media, cleft palate, tissue mechanics, middle ear, histological image, computational modeling, computation fluid dynamics, finite element analysis, fluid-structure interaction

# I. Introduction

One of the most commonly diagnosed childhood illnesses is a disease called Otitis Media (OM). This disease is characterized by pain and inflammation of the Middle Ear (ME). OM affects thousands of patients per year and has an annual health-related cost of four billion dollars in the United States [1]. The persistence of OM has been directly related to dysfunction of a patient's Eustachian Tube (ET).

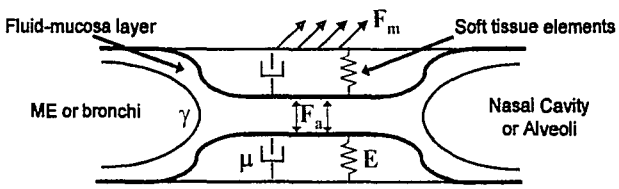


**Figure 1: Engineering Model of the Eustachian Tube**

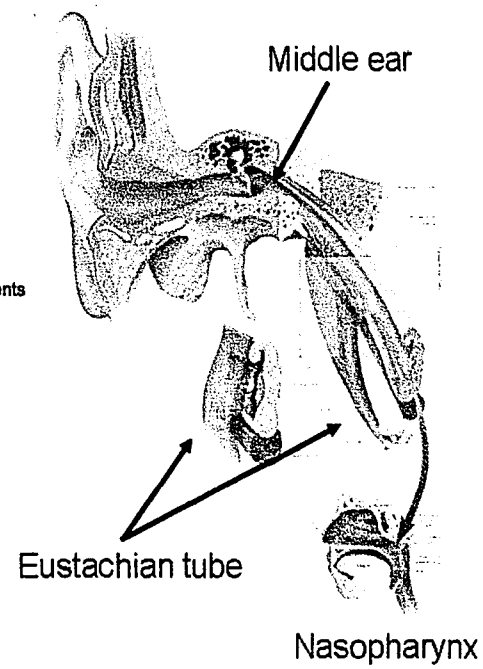


**Figure 2: Anatomy of the Eustachian Tube**

The ET is a collapsible tube that connects the ME and the Nasopharynx (NP) (Figure 2). The ET is responsible for three primary functions: 1) regulation of ME pressure 2) protection of the ME from foreign pathogens and 3) drainage of fluid from the ME [2]. The ET is structurally homologous with the small pulmonary airway that connect alveoli and the larger bronchial airways. Specifically, the lumen of these collapsed airways contains a fluid-mucosa layer and is surrounded by viscoelastic soft tissue elements

(Figure 1). The ability to open these airways will therefore depend on both tissue mechanical properties (e.g. applied muscle forces, $F_m$, and tissue elasticity, E and viscosity, $\mu$) and micro-scale, adhesive properties within the mucosa (e.g. molecular adhesion forces, $F_a$, and surface tension forces, $\gamma$). In healthy patients, the ET opens during swallowing because the surrounding tissue is deformed by muscle activity. If the ET fails to open, the ME develops painful sub-ambient pressure. As a result, liquid is then pulled in from the mucosal tissue surrounding the middle ear. This can result in fluid accumulation within the ME and any bacteria present in the accumulated fluid are provided with an environment that is perfect for infection to develop. Standard practice for treating ET dysfunction includes having a ventilation tube inserted through the eardrum [2]. This procedure relieves the symptoms of ET dysfunction, however the procedure has some adverse effects. A perforation in the tympanic membrane can lead to hearing loss and provides an accessible pathway for foreign material and infectious agents. Furthermore, these ventilation tubes typically fall out within 3-4 months and can therefore require repeated surgeries.

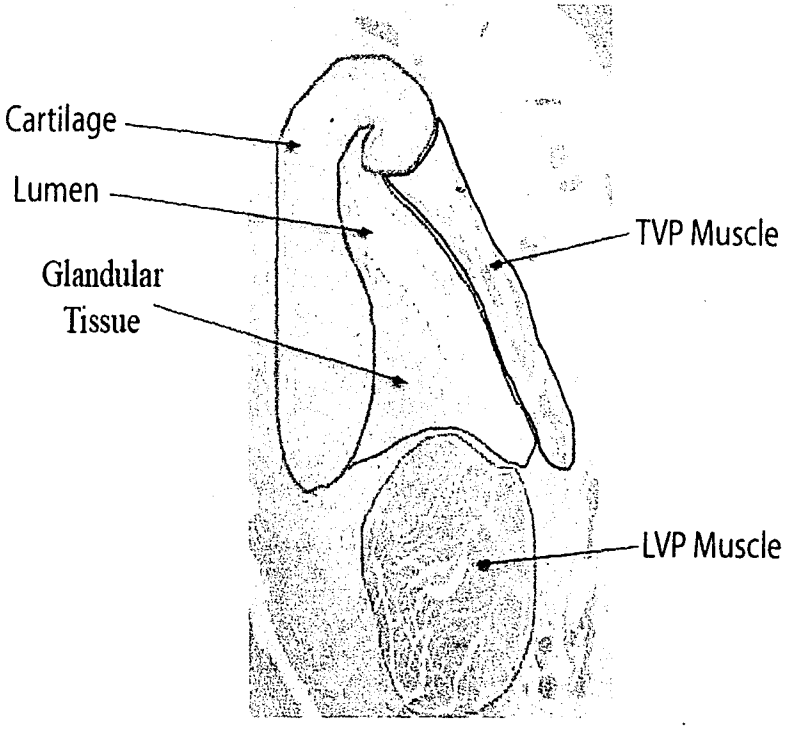


**Figure 3: Cross sectional slice of the Healthy Adult Eustachain Tube**

The ET is a complex, three dimensional structure made of primarily cartilage and glandular tissue surrounded by bone and muscle as seen in Figure 3. There are two primary muscles that act on the ET, the tensor veli palatini muscle (TVPM), and the levator veli palatini muscle (LVPM). The TVPM is a ribbon-like or flat muscle that attaches to the cartilage and glandular tissue at one end and then wraps around the Pterygoid Hamulus at the other end. The LVPM is a muscle bundle that runs along the length of the ET and expands during contraction, such that it exerts normal or distributed forces on inferior portions of the cartilage and glandular tissue. There are several factors that can influence ET function, the first of which are the magnitudes and directions of the forces generated by the TVPM and LVPM. Previous investigations have demonstrated that if the TVPM is paralyzed, the ET will fail to open [3]. Another factor in ET function is the compliance and/or elasticity of the surrounding tissues, as displayed in Figure 1. For example, if the cartilage and/or glandular tissue are too stiff, the forces exerted by the

TVPM cannot deform the tissue and generate an opened lumen. Conversely, if the cartilage and/or glandular tissue are too soft, the forces generated by the TVPM may not be transmitted to luminal surfaces and as a result, muscle contraction may not generate the luminal forces needed to overcome the adhesion forces that maintain a closed ET. In either way, abnormal mechanical properties of the ET soft tissue elements can significantly compromise ET function. Finally, another important factor is the position of the Hamulus, since the position of the Hamulus governs the direction vector of the TVPM forces. Moving the Hamulus distally, laterally, or superiorly can have either adverse or positive effects on ET function.

There have been previous investigations, including computational and experimental studies, into the mechanics of ET function and dysfunction [5-9]. Bell, *et al.* [6] developed 2 dimensional finite element models of tissue deformation and lumen opening in order to simulate ET function in healthy adults. These models used one cross-sectional histological image similar to the one shown in Figure 3 to generate 2D solid models which captures the shape and size of ET tissues at one axial location. These 2D models were then used to simulate tissue deformation and lumen opening and a 1D fluid model was used to predict flow through the lumen [6]. This model has some obvious drawbacks. The first of which is that the solid model is only two dimensional. The ET is a complex three dimensional structure and a two dimensional model cannot accurately represent the morphology of the ET. Secondly, a 1D fluid model was used that assumed a constant pressure drop through the lumen and fully developed flow in the axial direction. Due to the lumen's complex shape, the assumptions that the pressure drop will be constant throughout the length of the lumen and that the flow is fully developed are

not likely to be valid. Warrick *et al.* developed three dimensional models to analyze ET dysfunction in cleft palate patients [7]. The main limitation of these models is that the fluid and solid domains were completely uncoupled. These models were therefore unable to capture the transient flow dynamics that occur during ET opening and closing.

Ghadiali *et al.* [8,9] developed two clinical tests, a Forced Response Test and a Modified Force Response Test, that can quantify ET function [8,9]. During the forced response test, a

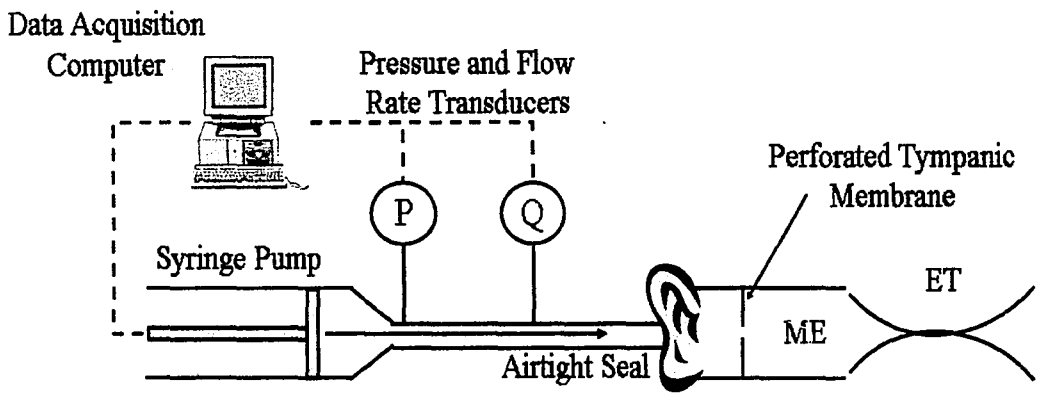


**Figure 4: Experimental Apparatus**

patient undergoes myringotomy (surgical incision through the ear drum), allowing externally applied pressure (P) to reach the ET. The patient's auditory canal is fitted with an experimental apparatus that contains a pressure transducer and mass flowrate sensor. The apparatus forms an airtight seal against the auditory canal allowing the ET to be inflated with externally applied pressure. A syringe pump applies 200 mm $H_2O$ of pressure through the auditory canal and ME into the ET establishing a baseline flowrate of air (Q). The patient is then asked to swallow. The action of swallowing causes contraction of the TVPM and LVPM which apply forces to the ET tissues and thereby producing a change in flowrate through the ET. This flowrate is recorded as a function of

time. In addition, changes in lumen pressure (P) are also recorded as a function of time. Then a parameter called resistance to flow, $R_v$ is calculated as pressure divided by flowrate (i.e. $R_v(t)=P(t)/Q(t)$). The resistance as a function of time, $R_v(t)$ can then be plotted as shown in Figure 5.

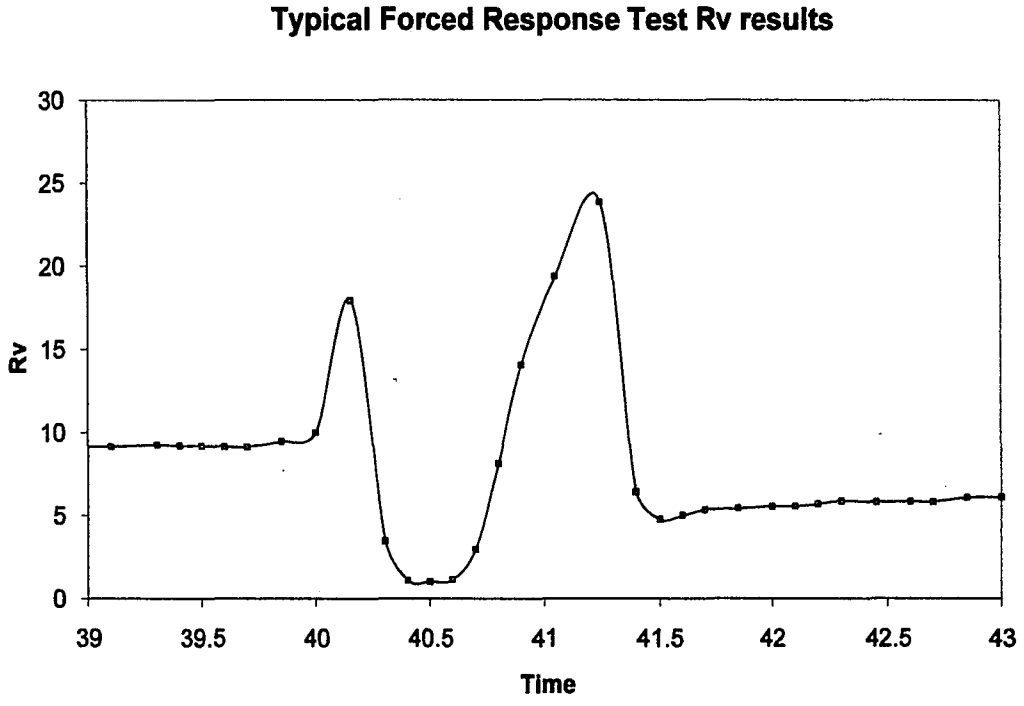


**Figure 5: Typical resistance plot form a Forced Response Test**

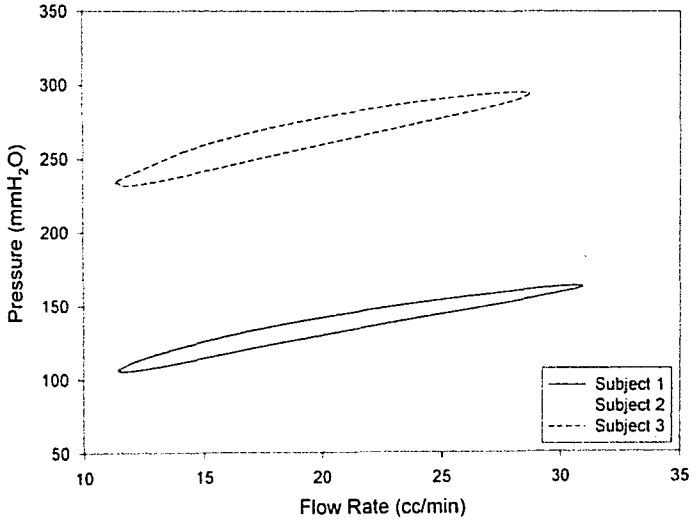


**Figure 6: Typical hysteresis loops from a Modified Forced Response Test**

The other test that can be performed on patients in a clinical setting is the Modified Forced Response test. During this test, the initial procedure is the same. The patient undergoes myringotomy and the same apparatus is inserted in the patients auditory canal. The syringe pump then applies 200 mm $H_2O$ of pressure establishing a baseline flowrate through the ET. Then, rather than having the patient swallow, the computer-controlled syringe pump is used to oscillate the externally applied pressure at a given frequency and the resulting flowrate is recorded. This produces a pressure curve that is a sine wave with specified amplitude and frequency and a resulting flowrate curve that is a scaled, shifted sine wave relative to the pressure curve. Due to the phase lag between the pressure and flowrate wave forms, when you plot pressure versus flowrate for one cycle, the resulting graph is a hysteresis loop. Some typical hysteresis loops from modified force response tests are shown in Figure 6. As seen in Figure 1, the hysteresis loops can be quantified in terms of wall compliance, $C = \frac{1}{E}$, and wall viscosity, $\mu$. As in Ghadiali *et al.* [8], the compliance of the ET has a direct impact on the overall slope of the hysteresis loop, while ET wall viscosity has a direct effect on the area contained inside the hysteresis loop. Subjects with higher compliance show much shallower slopes than subjects with a less compliant ET. Increasing the wall viscosity introduces more visco-elasticity thus making the loops contain more area. These two clinical tests show the transient dynamics that occur within the ET during opening and closing. Figure 5 and Figure 6 graphically demonstrate the different types of transient dynamic phenomena that decoupled models, such as the ones developed by Warrick *et al.* [7], cannot capture and therefore may not be able to accurately analyze/interpret ET function from experimental

data. Therefore, there is a need to develop fully coupled fluid-structure interaction (FSI) models of ET function that can simulate experimental conditions.

This paper outlines two separate studies that share the common result of improving our understanding of ET function and dysfunction. First, Chapter II describes the methodology and results from a parameter variation studies done on healthy adults and cleft palate patients. Using decoupled FE models of 6 different patients with a cleft palate, the parameters that can possibly affect ET function were symmetrically varied to find their respective sensitivity to ET function. Secondly, Chapter III describes the methodology and results from two fully coupled, FSI models, one of a healthy adults and one of a cleft palate infant. Using these two models, a study is performed that varied relative muscle timing to see its possible impact on ET function. Third, new modeling efforts and new FEM techniques are outlined that make the previous models even more advanced. Finally, the conclusions chapter summarizes what both studies have taught us about ET function.

## II. Decoupled Finite Element Analysis (FEA) Modeling

### A. Methodology

In the first part of this study, we analyze both healthy adult and cleft palate patients using the procedures described in previous studies [7]. First, histological data of the ET soft tissue structure is obtained from the University of Pittsburgh's Otopathology laboratory located within the Children's Hospital of Pittsburgh. The histological specimens are processed based on the method developed by Sando et. al [4]. Cross-sections are sliced perpendicular to the long axis of the ET after being fixed in formalin, decalcified with trichloroacetic acid and dehydrated in ethanol. The cross-sections are cut every 30μm and every 20$^{th}$ section is stained with hematoxylin and eosin. The specific area of the histological slide of interest includes the ET cartilage, TVPM, LVPM and glandular tissue (as shown in Figure 7).

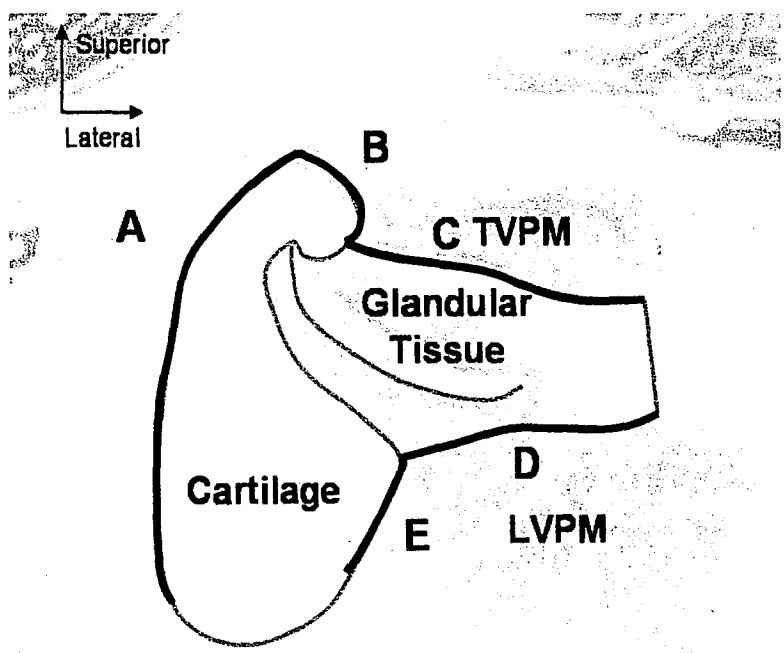


**Figure 7: A sample histological cross section showing outlines and sections**

The histological cross-sectional images are analyzed using the image analysis procedure described by Ghadiali et al.[5]. Briefly, the MetaMorph image analysis software (Sunnyvale, CA) is used to obtain outlines of the different tissue elements; cartilage, glandular tissue, lumen, TVPM and LVPM (see Figure 7). The attachment of the cartilage to the cranial base is identified, to be used as a boundary condition, as section A. The areas where the TVPM is acting on the cartilage and glandular tissue are shown in Figure 7 as sections B and C respectively. The areas where the LVPM acts on the cartilage and glandular tissue is shown as sections E and D respectively. During this process the lumen is artificially opened due to tissue dehydration. However, the models are constructed with a closed lumen to better simulate *in-vivo* conditions. In all these models, the lumen is drawn with respect to the medial edge of the artificially opened lumen as shown in Figure 7.

This process is repeated for each sequential cross section along the distal axis of the ET starting from the ME and moving toward the NP. Figure 8 is one example of how the geometry of the ET changes along the distal axis from the ME (Figure 8A) to the NP (Figure 8C).

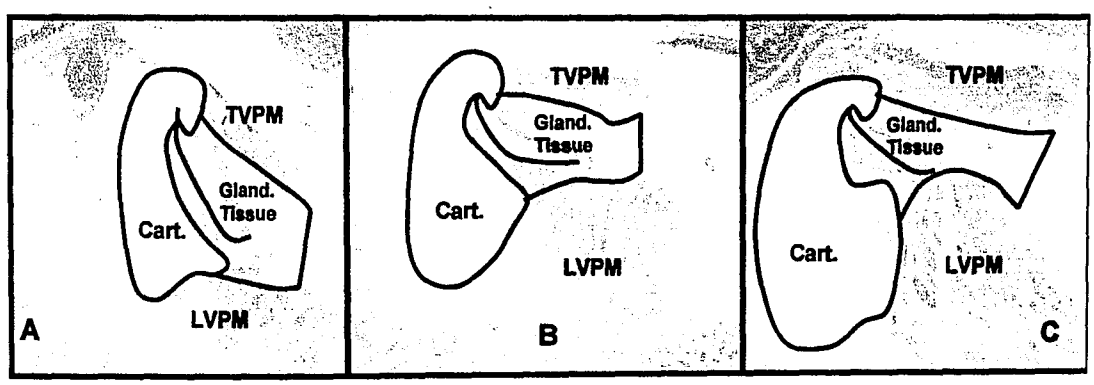


**Figure 8: Histological cross sections of the ET showing distal geometry changes.**

Some patients show more drastic geometry changes along the distal axis, which is why the three dimensional modeling procedure is so important.

Outlines obtained in sequential axial images are used to generate a 3D solid model in Pro/Engineer CAD program (Needham, MA) of the cartilage and glandular tissues. A cubic spline algorithm is used for each subject to generate smooth lofted surfaces between the cross-sections. Each section (A-E, Figure 7) is converted into a 2D surface in order to facilitate the application of boundary conditions and loads. Once the solid model is created, it is ready to be loaded into the FEA program.

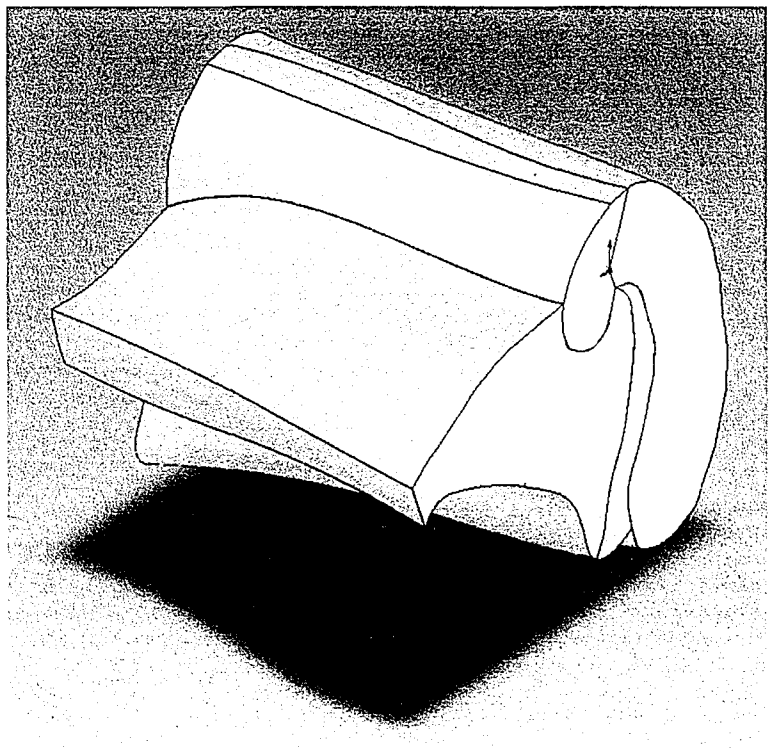

**Figure 9: 3D CAD model P847 Eustachian Tube**

The basis of Finite Element Analysis is that the differential equations which govern tissue deformation in the solid domain or fluid flow in the fluid domain are solved over a series of finite elements rather than over the domain as a whole. To do this, the geometry is broken down into a system of points, or nodes, that are connected into

individual elements to create a mesh that represents the original structure. Then material properties are assigned to each element so that the mesh accurately represents both the original geometry and the type of tissue simulated. An example mesh can be seen in Figure 10. The Finite Element program chosen for all the analysis is ADINA (Watertown, MA).

In these cleft palate models, the cartilage and glandular tissue are both modeled as a Mooney-Rivlin hyperelastic material. This material model is based off of the following expression.

$$W_D = C_1(I_1 - 3) + C_2(I_2 - 3) + C_3(I_1 - 3)^2 + C_4(I_1 - 3)(I_2 - 3) + C_5(I_2 - 3)^2 + C_6(I_1 - 3)^3 + C_7(I_1 - 3)^2 + C_8(I_1 - 3)(I_2 - 3)^2 + C_9(I_2 - 3)^3 + D_1 e^{D_2(I_1 - 3)} - 1 \quad (1)$$

where $W_D$ is the strain energy density and $C_1$-$C_9$, $D_1$, and $D_2$ are material constants, $I_1$ and $I_2$ are strain invariants as defined as by Bathe [17]. This form of the strain energy density assumes an incompressible material, $I_3$=1, and is further modified depending on 3D, plane strain, or axisymmetric analysis. The bulk modulus $\kappa$ is used to model the compressibility of the material. ADINA uses a default form for the bulk modulus based on small strain, near-incompressibility defined as

$$\kappa = \frac{E}{3(1 - 2\upsilon)} \quad (2)$$

where E is the modulus of elasticity and $\upsilon$ is the Poison's ratio. For both the cartilage and glandular tissue, $\upsilon_{cart}$=$\upsilon_{gland}$=0.499, where $\upsilon$=0.5 is an incompressible material. The bulk modulus can also be written in terms of a small strain shear modulus, G [16]

$$\kappa = \frac{2G(1 + \upsilon)}{3(1 - 2\upsilon)} \quad (3)$$

These moduli can be used to define a standard two-parameter Mooney-Rivlin strain energy density function

$$W = \frac{G}{2}(J_1 - 3) + \frac{\kappa}{2}(J_3 - 1)^2 \quad (4)$$

Here $J_1$ and $J_3$ are reduced strain invariants as defined as by Bathe [17]. The baseline elastic modulus for the cartilage and glandular tissue for the CP subjects was found in literature to be $E_{cart}$ = 150 kPa and $E_{gland}$ = 25 kPa [5,10]. In previous studies using healthy adult patients the elastic moduli were found in literature to be $E_{cart}$ = 300 kPa and $E_{gland}$ = 50 kPa [11,12]. Literature data [13] found that in infants and young children the modulus of elasticity is twice as compliant than in adults, which is why the values of 25 kPa and 150 kPa were chosen. Solving the 3D tissue deformation equations during ET opening phenomena required the use of a non-

linear, large displacement finite element routine [17]. The equations to be solved are

$$\frac{\partial \sigma_{ij}^S}{\partial x_j} = 0, \quad \sigma_{ij}^S = \frac{1}{2}\left(\frac{\partial W}{\partial \varepsilon_{ij}} + \frac{\partial W}{\partial \epsilon_{ji}}\right), \quad \varepsilon_{ij} = \frac{1}{2}\left(\frac{\partial d_i}{\partial x_j} + \frac{\partial d_j}{\partial x_i}\right) \quad (5)$$

Here $\sigma^S$ is the Cauchy stress tensor, W is the strain energy density, $\varepsilon$ is the strain, and $d_i$ is the displacement of each mesh node. However, before the equations can be solved, boundary conditions and forces must be applied. The main boundary condition in the model comes from the attachment of the ET to the cranial base as modeled by Section A in Figure 7. On this surface of the model, a boundary condition of zero displacement in all directions is applied because this tissue is fixed to bone. The other boundary condition represents attachment to bony portions of the ET via tendons which allow for in-plane displacements only. Therefore a boundary condition of zero displacement in the z-direction is specified only on the proximal and distal ends. In all models, the rotational DOF are not allowed, the model is only capable of linear displacements. The boundary conditions placed in the model are summarized in Figure 10.

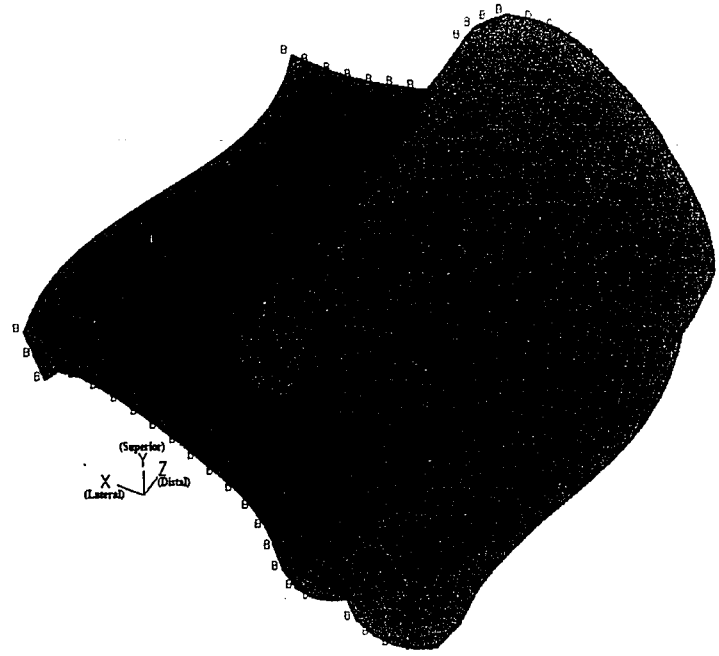


**Figure 10: FE model of ET of CP infant P847 with the applied boundary conditions**

In Figure 10, the boundary condition for the cranial base is applied to every node labeled with a C, and the proximal and distal condition is applied to every node labeled with a B. Also in the model, the force from the TVPM and the LVPM need to be represented. The TVPM is a ribbon like muscle that extends from the superior faces of the glandular tissue and the cartilage and then wraps around the pterygoid hamulus [14]. The LVPM pushes up on the inferior surfaces of the glandular tissue and cartilage. The TVPM and LVPM forces need to be adjusted for the infant models. It is not appropriate to apply the same amount of force on the smaller models that is applied to the larger models. From previous research, it has been found that the amount of force the muscle applies is linearly proportional to the cross sectional area of the muscle [15]. The cross sections of the muscle for all the different models are measured using MetaMorph. It was found that the ratio of cross sectional areas of both TVPM and LVPM for adults to CP infants was 1:0.5. In previous ET study, 20N and 5N were used for the TVPM and LVPM,

respectively in healthy adults. Therefore, values of 10N and 2.5N were used for the CP infants based on the muscle area ratio. The LVPM and TVPM muscles are both visualized in Figure 11.

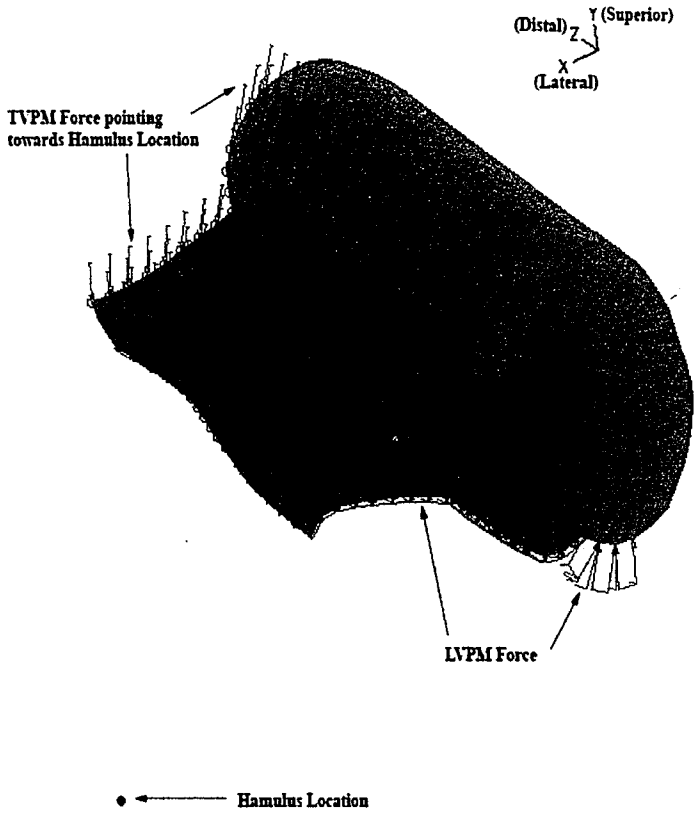


**Figure 11: FE model of ET of CP infant P847 showing the TVPM and LVPM Forces**

In the above figure, note how the force vectors due to the TVPM all point to the same physical point in space, the pterygoid hamulus. The TVPM load is a follower load so it is displacement dependant. As the solid model deforms, the vectors change direction so they are always pointing the pterygoid hamulus location. The LVPM load is modeled as a pressure, normal to the surface that is also displacement dependant.

The model is now fully defined and can be solved. Solving equation (5) yields a deformed solid model that now has a lumen opening as shown in Figure 12.

[illegible] respectively for the young adult. Intermediate values of 1.0N and 2.5N were used for the CPM [illegible] muscle area ratio. The LVPM and TVPM muscles are both [illegible]

[illegible]

[illegible]

Figure 11. Extended Finite Element Model showing the LVPM and TVPM Forces

[illegible] Figure 11, now how the force vectors due to the TVPM all point to the same [illegible] point in space, the pterygoid hamulus. The TVPM load is a follower load so it is [illegible] dependant. As the solid model deforms, the vectors change direction so [illegible] are always pointing the pterygoid hamulus location. The LVPM load is modeled as [illegible] normal to the surface that is also displacement dependant.

The model is now fully defined and can be solved. Solving equation (5) yields a deformed solid model that now has a lumen opening as shown in Figure 12.

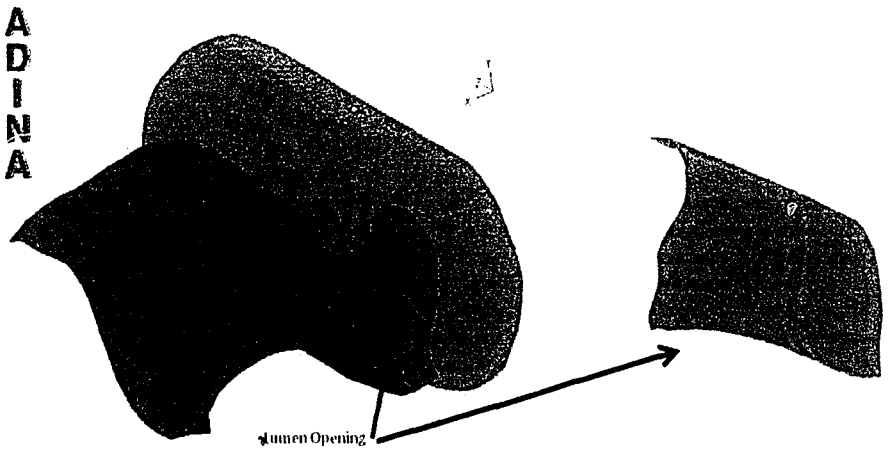


**Figure 12: Deformed solid model with extracted lumen opening**

Once the solid model is deformed, the lumen opening must be extracted out of the model. In previous research [6], a 1D fluid model was used to quantify flow through the deformed shape. The 1D model assumed fully developed flow with a linear pressure gradient. Due to the complex 3D geometry, a linear pressure gradient is a very large assumption and might not necessarily be true. In this study however, 3D computational fluid dynamics (CFD) is used. CFD can take into account the complex geometry with no assumptions about pressure gradients or fully developed flow therefore giving the most accurate results. To extract the deformed lumen shape form the solid model, a series of scripts are used in MatLab, then TecPlot, then Rhinoceros to make the lumen geometry which defines the CFD or fluid domain. The resulting lumen that was extracted out of the deformed solid model is also shown in Figure 12.

In the extracted lumen opening, flow is governed by the incompressible continuity and Navier-Stokes equations

$$\rho\frac{\partial v_i}{\partial x_i} = 0 \; and \; \rho\frac{\partial v_i}{\partial t} + \rho v_j\frac{\partial v_i}{\partial x_i} = -\frac{\partial p}{\partial x_i} + \mu\frac{\partial^2 v_i}{\partial x_i x_j} \qquad (6)$$

where $\rho$ is the density of air, 1.229 kg/m$^3$, $\mu$ is the viscosity of air, 1.8x10$^{-5}$ Pa·s, and $v$ is the velocity vector. To quantify ET function, the same pressure drop was applied to all lumen openings, 200 mm $H_2O$ from ME to NP. To accomplish this, no slip boundary conditions are applied to all the walls of the lumen, a normal traction of 1961 Pa is applied to the ME side (least distal) opening of the lumen, and a zero pressure condition is applied to the NP side (most distal) of the lumen. The flowrate is found by integrating the velocity profile at a specified cross section in the middle of the lumen.

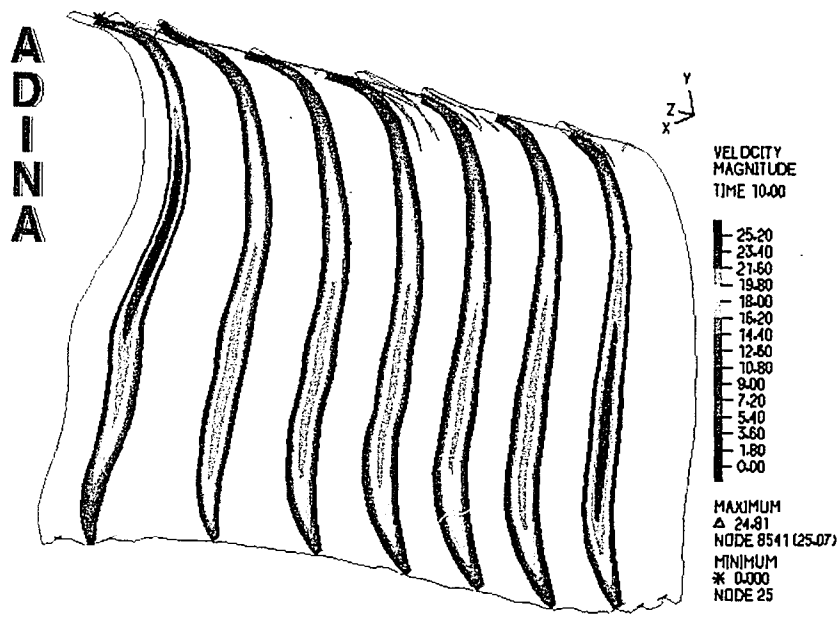


**Figure 13: Cross sections of velocity profile in the lumen opening**

Figure 13 shows the typical velocity profiles at different cross sections down the distal axis of the lumen. The typical velocity scale through the lumen is on the order of 25 m/s, which gives a maximum Re of 335 in healthy adults. Given this maximum value of Re, which represents the ratio of inertial to viscous forces, the flow is in the laminar regime. Once the flowrate in the lumen was determined, the degree of lumen opening was quantified by calculating a flow resistance parameter,

$$R_v = \frac{\Delta P}{Q} \quad (7)$$

where ΔP is the pressure drop from the ME to the NP, and Q is the flowrate. Note that larger values of $R_v$ represent ET dysfunction while smaller values of $R_v$ represent better ET function.

The reason for calculating Rv is to facilitate comparison with the experimentally measured data.

To quantify how sensitive ET function is to a specific parameter, a new quantity, sensitivity, is defined. For this parameter variation study, the sensitivity is defined as the ratio of the resistance value at the baseline parameter divided by the resistance value at 4 times the baseline parameter value.

## B. Parameter Variation Studies

For a healthy adult, a full parameter variation study was done for one patient where the parameters varied were TVPM force magnitude, LVPM force magnitude, Young's modulus of Cartilage, Young's modulus of glandular tissue, Hamulus X position, Hamulus Y position, Hamulus Z position. The range of the seven parameters is given in Table 1.

**Table 1: List and ranges of parameters varied for study**

| Parameter | $E_{cart}$ | $E_{Gland}$ | TVP | LVP | Ham X Pos | Ham Y Pos | Ham Z Pos |
|---|---|---|---|---|---|---|---|
| Min Value | 75.4 kPa | 31.5 kPa | 5 N | 0.5 N | Original Location | Original Location | Original Location minus 10% |
| Max Value | 3000 kPa | 500 kPa | 50 N | 8 N | 100 % Lateral Movement | 100 % Superior Movement | 120 % Distal Movement |

For this study, $E_{Cart}$ and $E_{Gland}$ were both varied from their minimum up to their maximum value in 8 increments. TVPM and LVPM magnitudes were varied over 10 increments.

Lateral and Superior movement of the hamulus location was varied from its original location up to 100% of the available lateral/superior measurement. More specifically, if all the tissue that comprises the ET measured 5 mm in the lateral direction at its widest point, then the hamulus point was allowed to vary 5 mm laterally. The same procedure was applied to superior and distal movement of the hamulus position. Lateral and Superior movement were varied over 10 increments, while the distal movement was varied in 12 increments. In total, 68 simulations were run to compile all the data for this study.

In the cleft palate population, a study was done that varied the magnitude of the TVPM and the LVPM across 6 patients. The TVPM magnitude was varied from 4 N up to 40 N in 10 increments and the LVPM was varied from 0.25 N up to 10 N in 10 increments. In total, 120 simulations were done to compile the data.

## C. Results

### i. Healthy Adult Simulations

The results for the parameter variation study for the health adult are summarized in the following seven figures.

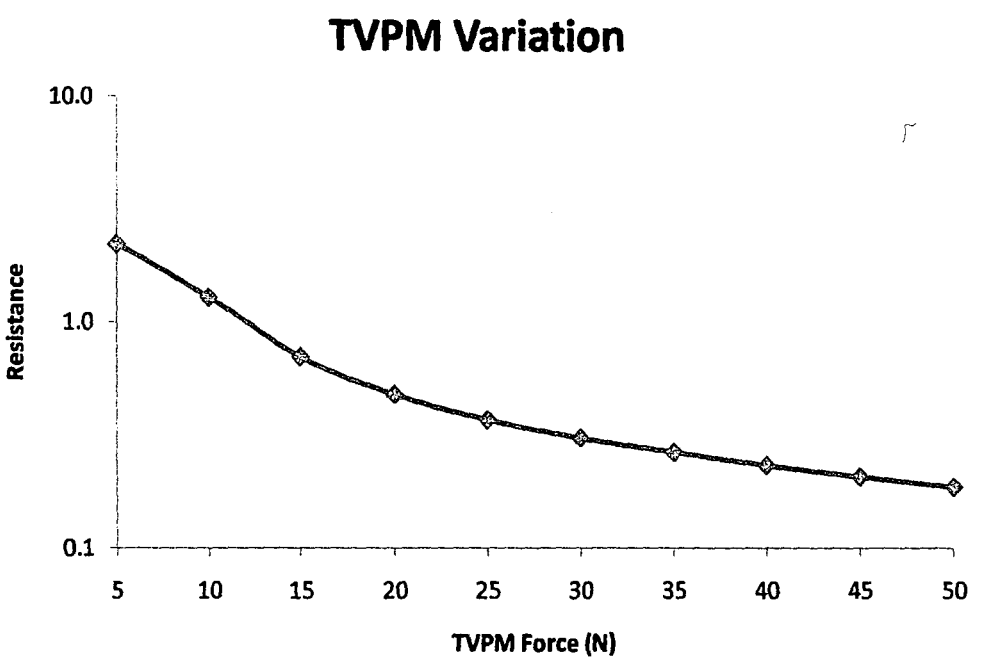


Figure 14: Plot of Resistance versus TVPM Magnitude

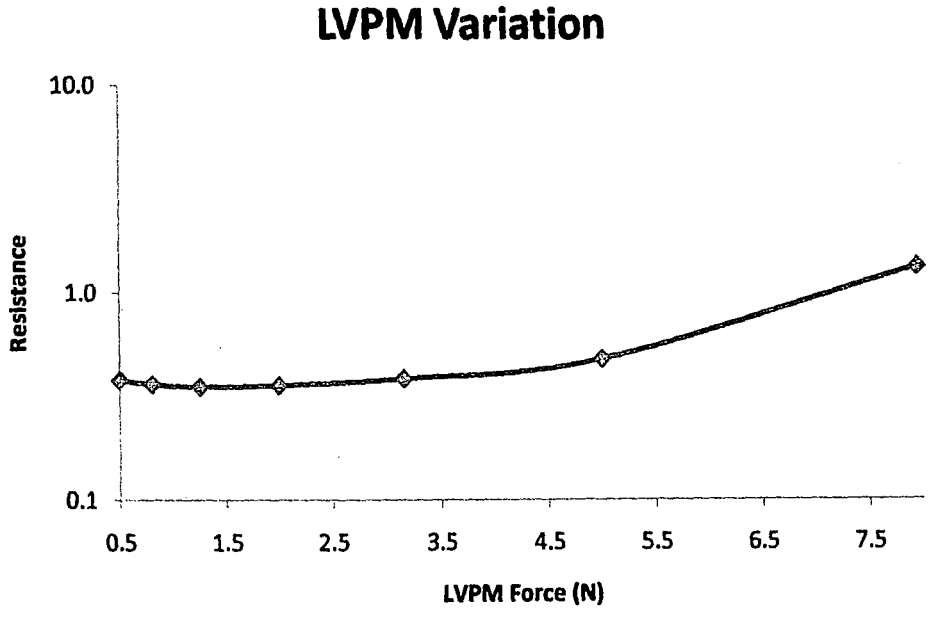


Figure 15: Plot of Resistance versus LVPM Magnitude

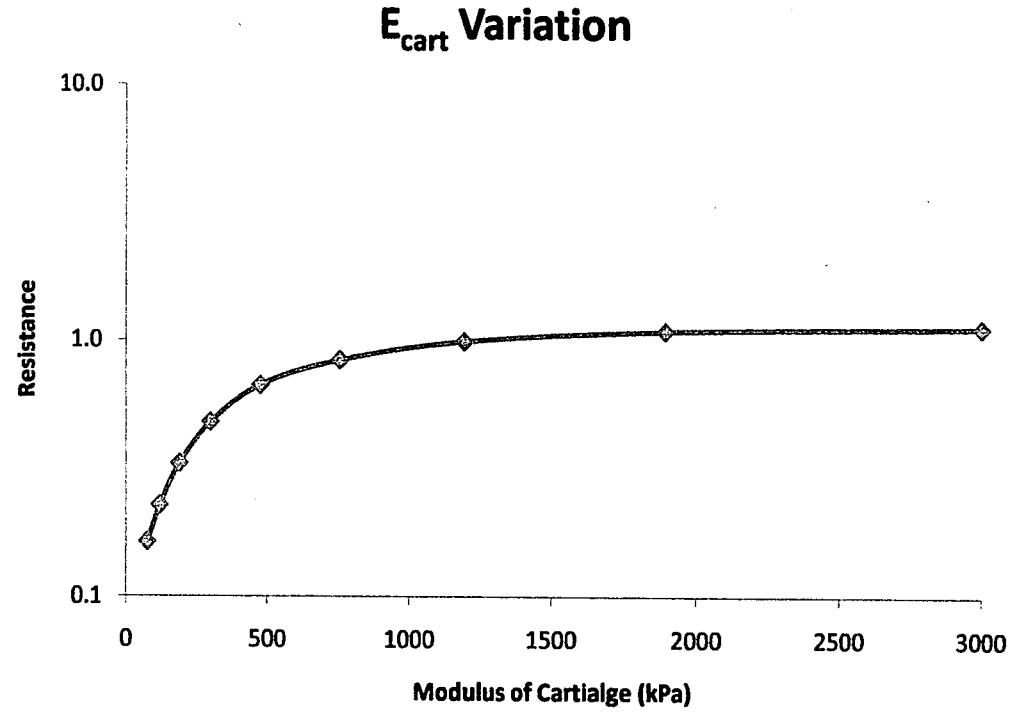


Figure 16: Plot of Resistance versus Modulus of Cartilage

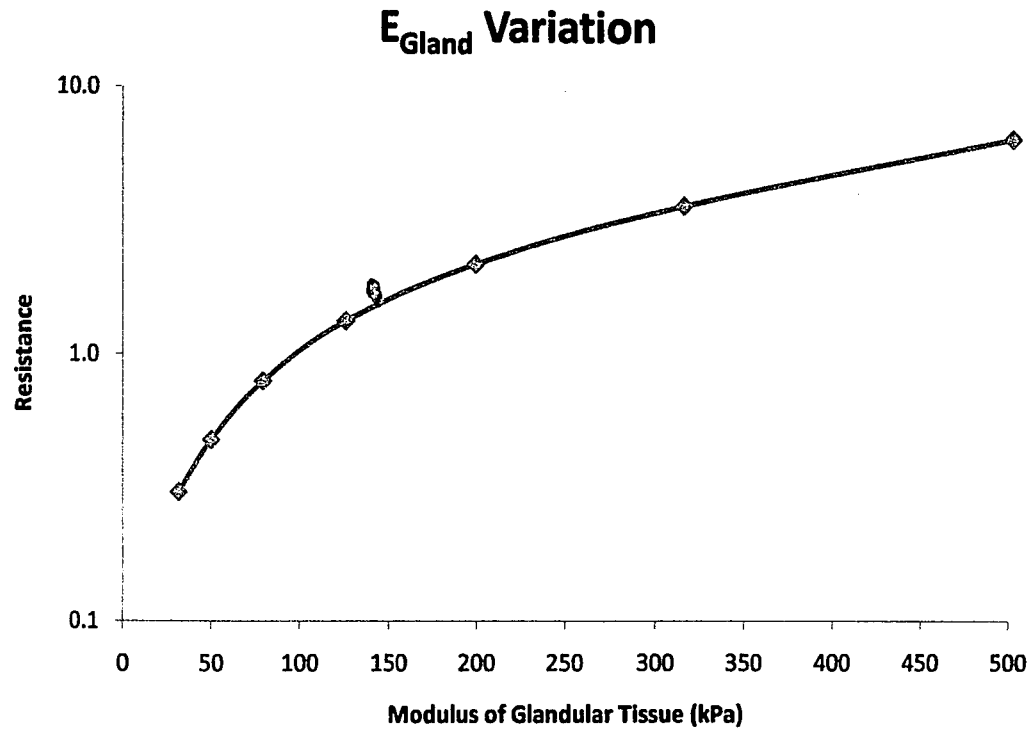


Figure 17: Plot of Resistance versus Modulus of Glandular Tissue

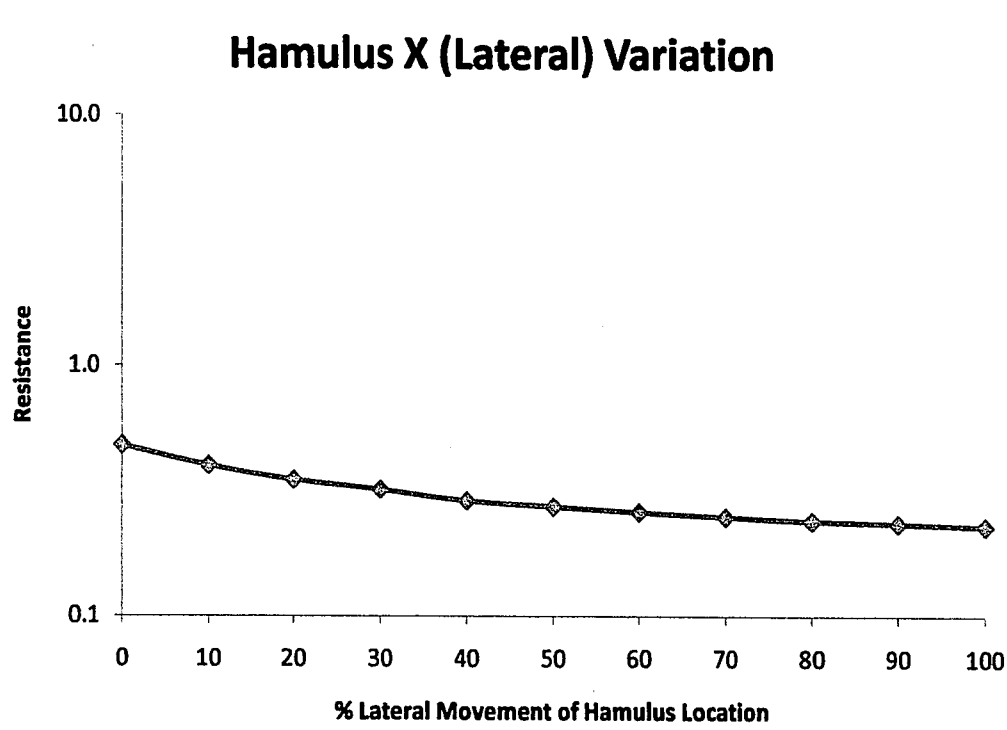


Figure 18: Plot of Resistance versus Hamulus X Location

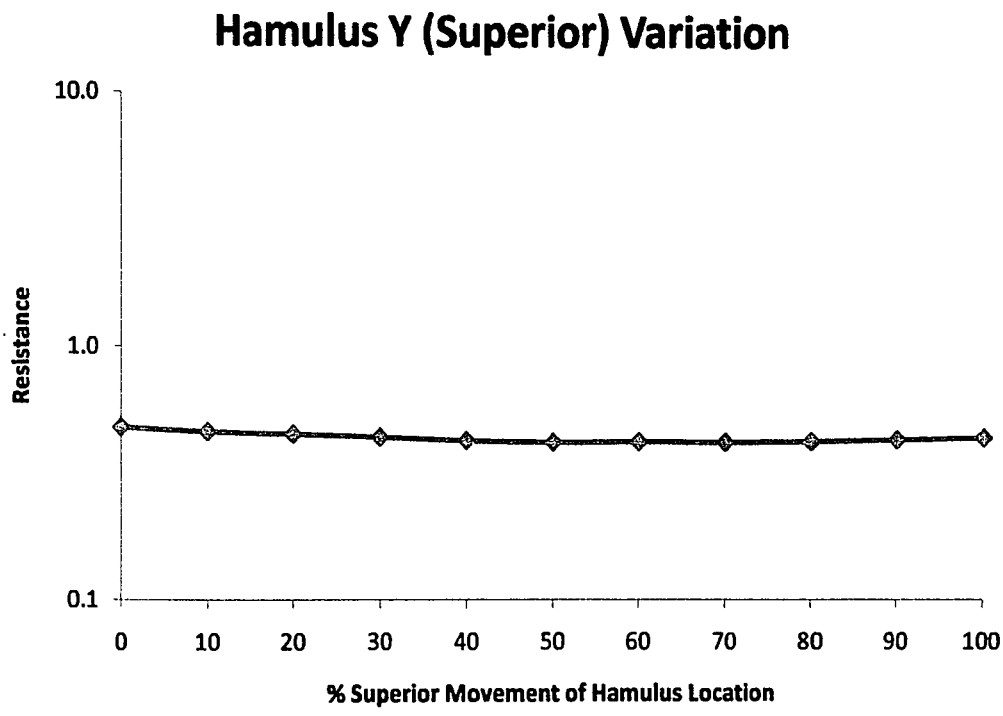


Figure 19: Plot of Resistance versus Hamulus Y Location

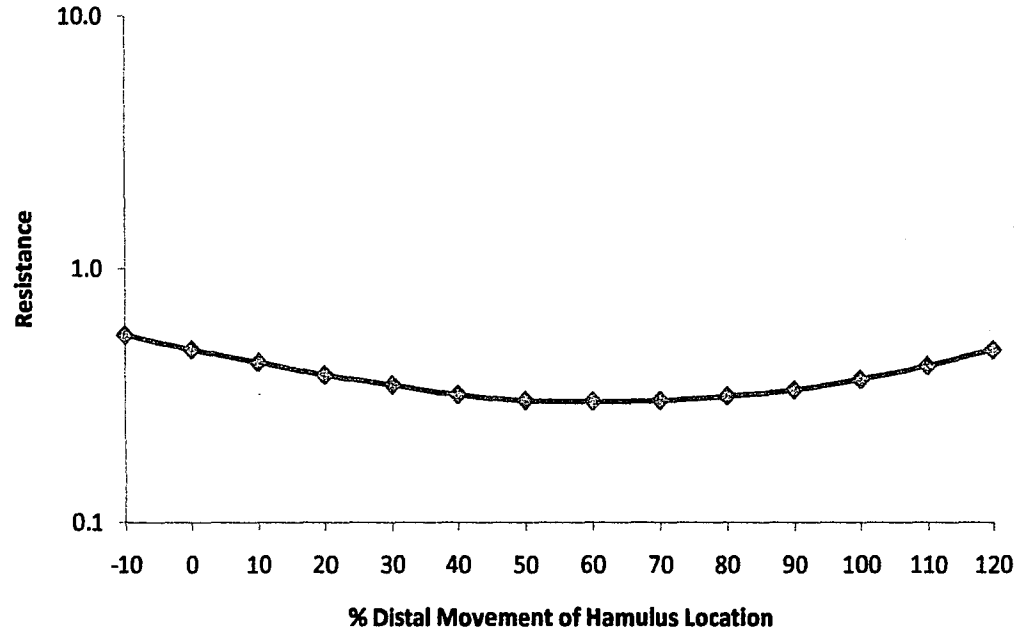


**Figure 20: Plot of Resistance versus Hamulus Z Location**

On the vertical axis of all the plots is the resistance to flow plotted on a log scale, and on the horizontal axis is the range of the parameter being varied. Looking at Figure 14, one can see that as the TVPM magnitude increases, the resistance values continually decrease. This is due to a larger lumen opening resulting from larger TVPM forces. However, looking at Figure 15, as the LVPM magnitude goes up, so does the resistance. This is due to the fact that the LVPM actually decreases the lumen opening and constricts flow. Looking at Figure 16, one can see that changing the modulus of elasticity of the cartilage has a large effect when the modulus is small, but then as the modulus grows, the sensitivity to the stiffness drops off. Physically, this makes sense since most of the lumen opening is contained in the glandular tissue, and only a small part of the opening is in the cartilage. Noting this fact also helps to explain Figure 17. Since most of the lumen opening is in the glandular tissue, it makes sense that the modulus of the glandular tissue

has a large effect on ET function. And finally, looking at Figure 18 through Figure 20, one can see that ET function is relatively insensitive to any changes in the hamulus position. Also, to reinforce these qualitative statements, Table 2 is a list of the parameters varied and their respective sensitivities, calculated as described at the end of Chapter II, Methodology section.

**Table 2: List of parameter and its respective sensitivity value**

| Parameter | Sensitivity |
|---|---|
| TVPM | 5.516 |
| LVPM | 1.061 |
| $E_{Cart}$ | 0.745 |
| $E_{Gland}$ | 0.217 |
| Lateral Hamulus Movement | 1.387 |
| Superior Hamulus Movement | 1.076 |
| Distal Hamulus Movement | 1.344 |

For sensitivity values, a value close to 1 corresponds to a graph whose line is relatively flat so the ET is insensitive to changes in this parameter. However, a sensitivity value much larger than 1 corresponds to a graph that has a negative slope meaning that as the parameter goes up in value, the resistance goes down in value. This implies that increasing the parameter has a positive effect on ET function. Then a sensitivity value much smaller than 1 corresponds to a graph that has a positive slope meaning that as the parameter goes up in value, so does the resistance. This implies that increasing the value of this parameter has a detrimental effect on ET function. So looking at all the values in Table 2, ET function is again most sensitive to TVPM magnitude and $E_{Gland}$, which agrees with the all the rest of the data.

### ii. Cleft Palate Parameter Variation Studies

The results from the cleft palate TVPM and LVPM magnitude variation study can be summarized in the following graphs.

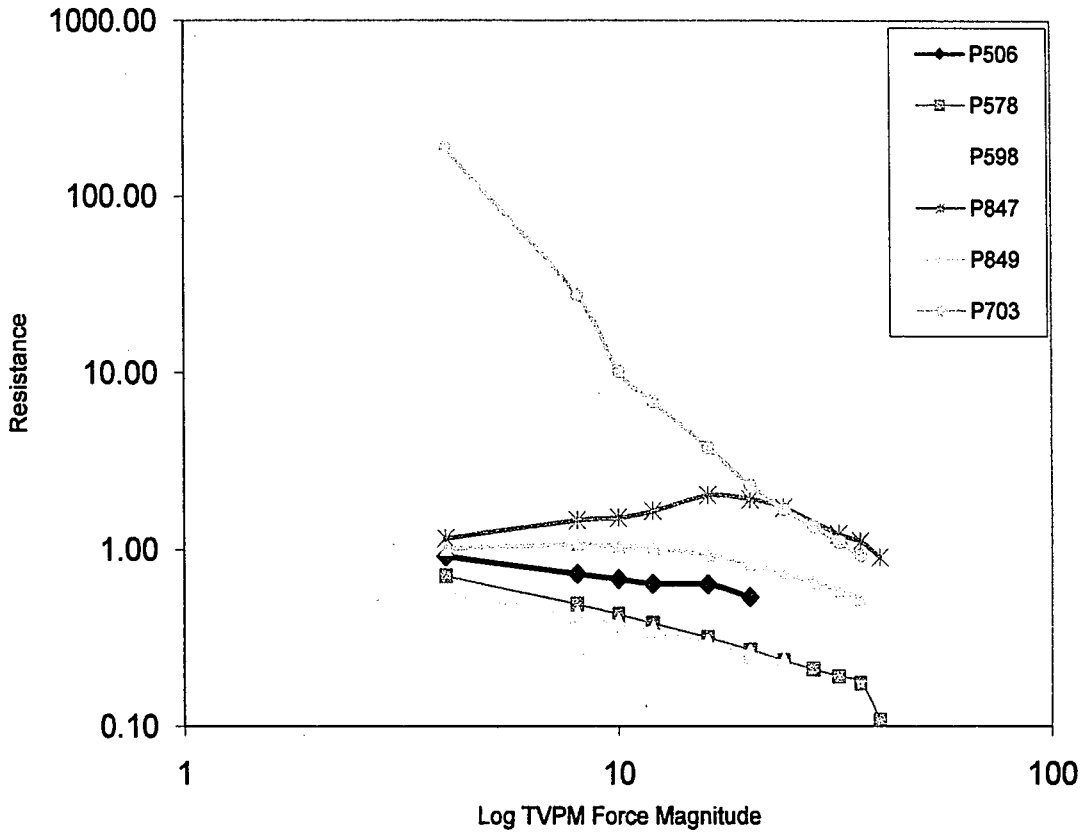


**Figure 21: Summary of Cleft Palate TVPM Variation Study**

Figure 21 is a plot of Resistance values on a log scale versus magnitude of TVPM force on a log scale. As the figure implies, all patients showed a reasonable amount of sensitivity to changing the TVPM force, however P703 showed extreme sensitivity to this muscle force change. Figure 22 is a plot of resistance values on a log scale versus magnitude of the LVPM force on a log scale. Again, P703 has much larger resistance values than all the other patients.

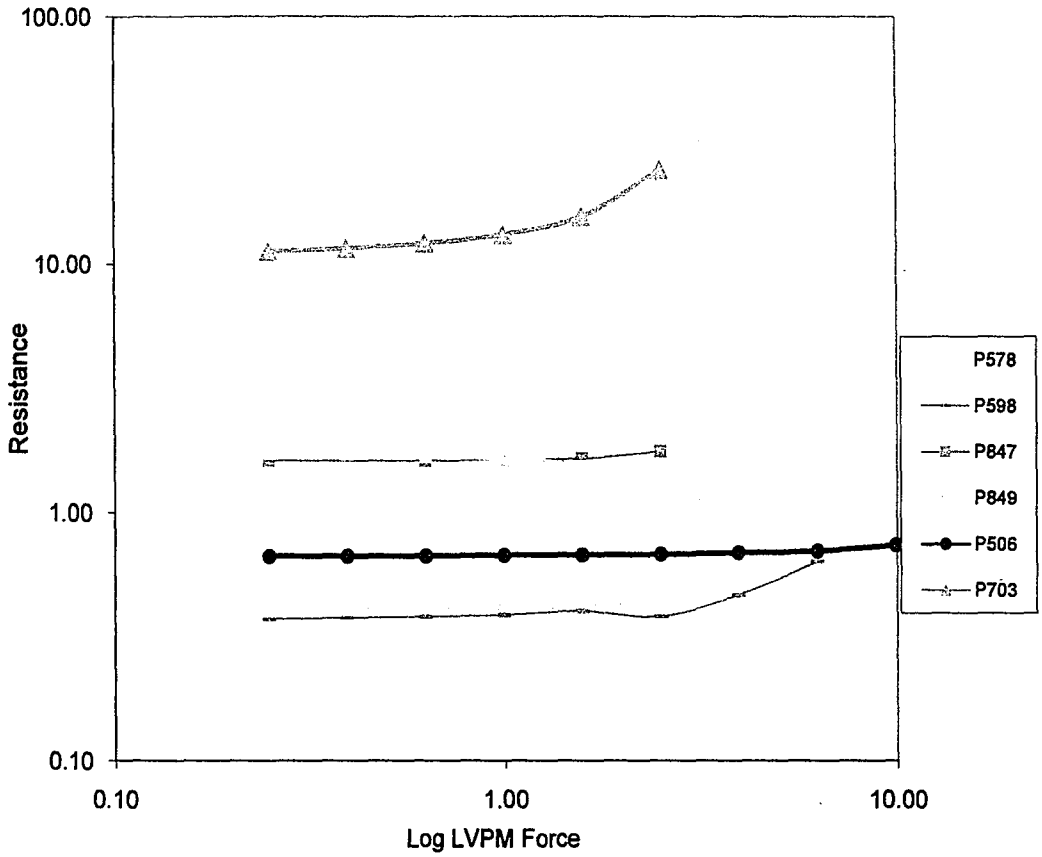


**Figure 22: Summary of Cleft Palate LVPM Variation Study**

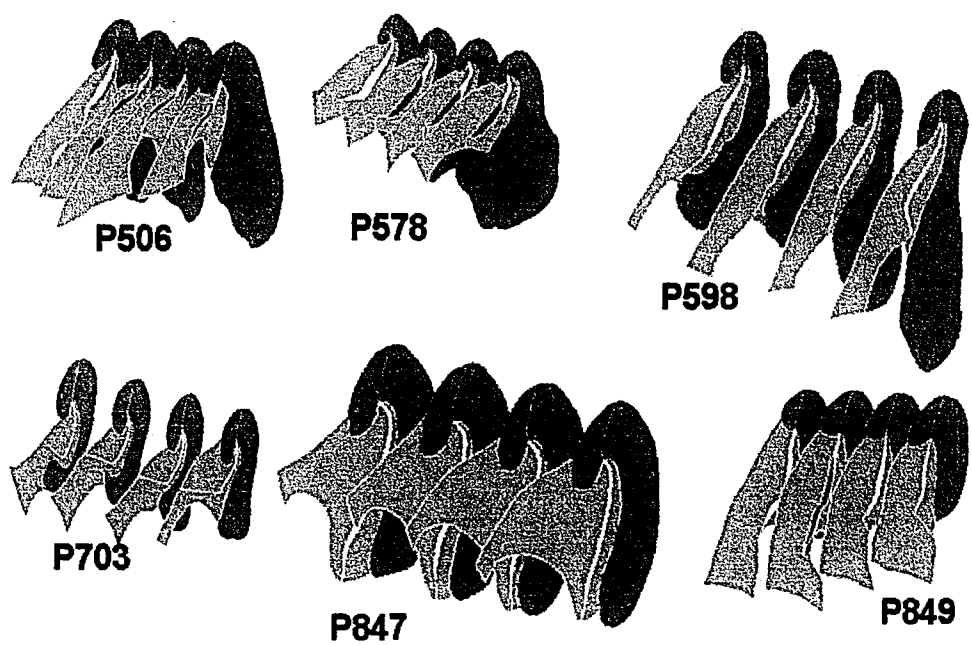


**Figure 23: Comparison of Cleft Palate Patient Morphologies**

In both Figure 21 and Figure 22, P703 is obviously an outlier. This can be explained by Figure 23. Looking at all the morphologies, it is clear that P703 has a much smaller lumen opening than all the other patients. This explains why the resistance values are so high for the same pressure drop. Since P703 is determined to be an outlier, it is not included in the following sensitivity calculations.

**Table 3: Summary of Cleft Palate Sensitivities**

| Patient | TVPM | LVPM |
|---|---|---|
| 506 | 1.44 | 0.993 |
| 578 | 2.23 | 0.997 |
| 598 | 1.94 | 0.964 |
| 847 | 0.57 | 0.993 |
| 849 | 1.11 | 1.051 |
| Average | 1.46 | 1.00 |

Looking at Table 3, you can see some variability among the patients, but overall, these numbers tell us that the degree of ET opening in cleft palate patients is less sensitive to TVPM and/or LVPM forces than in normal adults.

## D. Discussion

Patients with cleft palate disorder have a 100% incidence rate of dysfunction of the ET resulting in the development of chronic OM. Currently, surgeons do not take into account issues with the ET, such as the abnormal morphology or ET dysfunction, when performing the surgery to repair the hard palate. This study gives some insight into the mechanics of the ET and provides valuable information to the surgeons. By comparing the flow resistances of healthy adult patients to cleft palate patients, this study concludes what parameters are most effective in patient populations and highlights the differences between the models.

In the first part of this study, it was shown that the healthy adult patient's ET function was most sensitive to the magnitude of the TVPM and modulus of elasticity of

the glandular tissue. This is shown both in Figure 14 through Figure 20, and also numerically in Table 2. The high sensitivity value of the TVPM and low sensitivity value of $E_{Gland}$ prove that changing either of these two parameters had the largest effect on ET function. Given the sensitivity values, increasing the TVPM force or decreasing the stiffness of the glandular tissue has a positive effect on ET function.

In the second part of this study, it was shown that the cleft palate patients were insensitive to muscle force changes. Neglecting the outlier, P703 from the sensitivity calculations, Table 3 shows all the patients were completely insensitive to changes in the LVPM magnitude, while the TVPM sensitivities showed some variability, but on the whole, the population is insensitive to these changes as well.

Both of these results reinforce the original hypothesis that to fix the underlying ET dysfunction in cleft palate patients, the morphology has to be corrected.

## III. Fully Coupled Fluid-Structure Interaction (FSI) Modeling

### A. Methodology

The second goal of this thesis was to build FEA models that can capture the transient dynamics that occur during opening and closing of the ET. All the models built either in previous studies [6-7] or utilized in Chapter II were either two dimensional or the fluid and solid models were decoupled. As a result, these previous models could not capture the temporal dynamics of airflow within the ET during swallowing as recorded during experimental studies (see Figure 5 and Figure 6). Therefore, capturing the transient dynamics of ET function requires the development of new models that have a fully coupled solid and fluid domain so that the interactions between the two can be accurately simulated.

All the models built for previous investigations, as in Chapter II, Section A, were built with an initially closed lumen to better simulate *in-vivo* conditions of the tissue. To build a fluid-structure interaction (FSI) model, there needs to be a distinct fluid domain and a distinct solid domain present at all times in the model. To build an anatomically correct lumen opening, the original closed model was used and the lumen was inflated with a small amount of pressure so that a small opening would form. An alternative method to creating a distinct fluid domain would have been to redraw outlines on the histological slides to include the lumen opening due to dehydration. However, this technique would require the development of new image analysis procedures similar to the ones described in Chapter II, Section A. More importantly, since experimental studies use pressure to open an initially closed lumen, the first procedure will produce a more physiologically relevant lumen open as compared to the lumen opening due to

dehydration observed in the histological images. In addition, the first method was chosen because a great amount of effort was placed on drawing the outlines on the histological slides accurately so that the resulting models were a good representation of the true morphology of the patient. Redrawing all the outlines would not only take a lot of time, but could also lead to possible degradation of the accuracy of the models. Therefore, the method of creating an open lumen was chosen to be using the originally closed models from the previous study and using artificial lumen pressure to create an opening. The procedure for starting with an initially closed solid model and creating a FSI model is outlined below.

As shown in Figure 24A, all the muscle forces were taken off the model so the only force left was a lumen pressure while all the boundary conditions remained the same as described in Chapter II. This resulted in a deformed model as shown in Figure 24B.

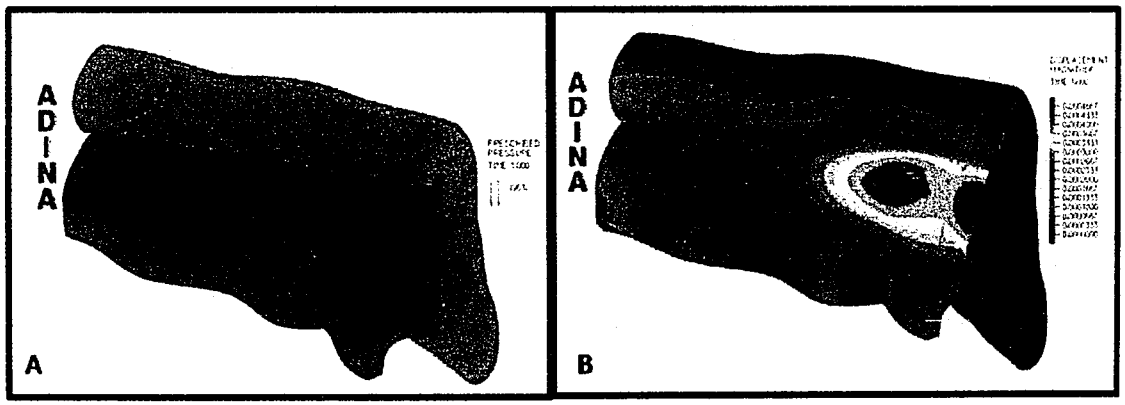


**Figure 24: FEA Model with only Lumen pressure to create an initial Fluid Domain**

Data was extracted from the deformed model and then run through a MatLab (Natick, MA) script that processed and rearranged the data. All the data was then imported into a FEA Post-Processing program, Tecplot (Bellevue, WA) which further processed the data and then extracted the boundaries of all the deformed bodies. All the data was then processed again with another MatLab script. This script is where most of the important

post-processing is done. The main purpose of the MatLab script is to read in all the data, interpret it and then export it to Rhinoceros 3.0 CAD software (Seattle, WA) in the proper way so that Rhinoceros can make three distinct solid bodies (cartilage, glandular tissue, and lumen). The MatLab script uses a custom programmed graphical user interface so the user can monitor what the program is doing, making sure that the geometry is correct and other important parameters are not being distorted. Once the MatLab script is finished processing the data, the Rhinoceros makes the 3D solid bodies and now the three bodies are ready to be imported into ADINA. Note that the three bodies include the cartilage, glandular tissue and lumen opening. The procedure that was outlined in the above paragraph has a few important points that should be noted. First, in Figure 24A, you will notice that there are four distinct color zones in the model. The procedure that is outlined in the decouple FEA models section creates four separate solid bodies, two to represent the cartilage, and two to represent the glandular tissue. The new procedure fixes this problem and creates one solid body that represents the cartilage and one solid body that represents the glandular tissue. This is more anatomically correct because in the decoupled models, you had to apply rigid link constraints between the two bodies that make up the cartilage and then apply rigid link constraints between the two bodies that make up the glandular tissue. By eliminating these constraints, the model is more anatomically correct and does not produce non-physiologic stress concentrations at body boundaries.

With a 3D CAD model of the cartilage, glandular tissue, and small lumen opening, all the components are in place to make a FSI model. In the FSI model, the

geometry is broken down into a solid and fluid domain. Each domain has its own distinct material models, boundary conditions, and loading.

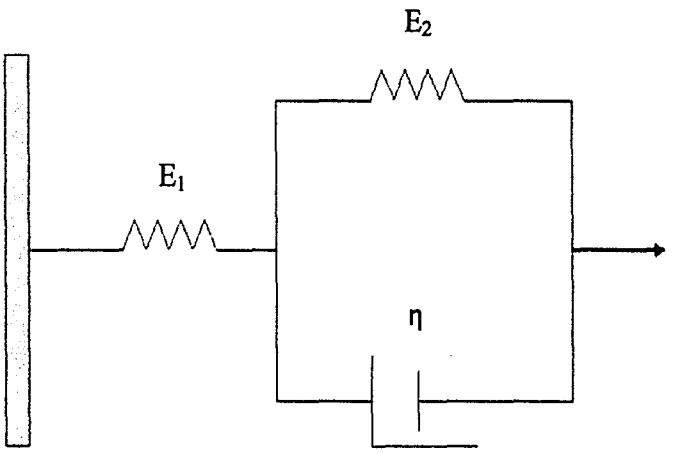


**Figure 25: Viscoelastic material model for the glandular tissue.**

In the solid domain, there are two different materials cartilage and glandular tissue. In the FSI model the cartilage is modeled as a Mooney-Rivlin hyper-elastic material just as in Chapter II, Methodology, equations (1) - (4). However, in the FSI model, the glandular tissue is modeled as a three parameter, viscoelastic material as shown in Figure 25. If $E_1$ were set to zero in this model, then the material would be equivalent to a Kelvin-Voigt solid. If $E_2$ were set to zero, then the material would act a Maxwell Fluid. For the ET model, it is chosen that $E_1=25 \cdot E_2$. Since the model is three parameter, choosing this relationship between $E_1$ and $E_2$ makes this material behave more like a viscoelastic solid which is appropriate since it is modeling tissue. Initial values of $E_1$, $E_2$, and $\eta$ were taken from previous studies [6], and these values are $E_1=9.38\text{x}10^6$, $E_2=3.75\text{x}10^5$, and $\eta=3.25\text{x}10^6$. To implement this model, it is known that the material satisfies the following convolution integrals.

$$s_{ij} = 2G(0)e_{ij}(t) + 2\int_0^t e_{ij}(t-\tau)\frac{\partial G(\tau)}{\partial \tau}\partial\tau \tag{8}$$

$$\sigma_{ij} = 2K(0)e_{kk}(t) + 2\int_0^t e_{kk}(t-\tau)\frac{\partial K(\tau)}{\partial \tau}\partial\tau \tag{9}$$

where σ is the stress, s is the deviatoric stress, e is the deviatoric strain, G is the Shear modulus, and K in the Bulk modulus, with the following definitions

$$s_{ij} = \sigma_{ij} - \frac{1}{3}\delta_{ij}\sigma_{kk} \tag{10}$$

$$e_{ij} = \varepsilon_{ij} - \frac{1}{3}\delta_{ij}\varepsilon_{kk} \tag{11}$$

$$\varepsilon_{ij} = \frac{1}{2}\left(\frac{\partial d_i}{\partial x_j} + \frac{\partial d_j}{\partial x_i}\right) \tag{12}$$

where $\varepsilon_{ij}$ is the strain and $d_i$ are displacements. For ADINA, the Bulk and Shear moduli are directly input as Prony-Dirchlet series as defined below.

$$G(t) = G_\infty + \sum_{i=1}^{N} G_i e^{-\beta_i t}, \text{and } K(t) = K_\infty + \sum_{i=1}^{N} K_i e^{-\beta_i t} \tag{13}$$

where $G_\infty$is the long time shear modulus, $K_\infty$ is the long time bulk modulus, and $\beta_i$. are the decay coefficients. For the ET material model, we use the leading term and then only the first term in the series, $G_1 e^{-\beta_1 t}$ and . $K_1 e^{-\beta_1 t}$, respectively. We calculate the terms in the Prony-Dirchlet series directly from the terms $E_1$, $E_2$, and η from the original material model as given by equations (14) through (20).

$$E_\infty = \frac{E_1 E_2}{E_1 + E_2} \tag{14}$$

$$E_A = \frac{E_1^2}{E_1 + E_2} \tag{15}$$

$$G_\infty = \frac{E_\infty}{2 + 2\nu} \tag{16}$$

$$G_A = \frac{E_A}{2 + 2\nu} \tag{17}$$

$$K_\infty = \frac{E_\infty}{3 - 6\nu} \tag{18}$$

$$K_A = \frac{E_A}{3 - 6\nu} \tag{19}$$

$$\beta = \frac{E_1 + E_2}{\eta} \tag{20}$$

In the solid domain, there exists one major boundary condition that represents the attachment of the ET to the cranial base of the skull. This is boundary condition of zero displacement on the lateral face of the cartilage. Just like in Chapter II, the TVPM force is a directional force that pulls to the Hamulus position and the LVPM force is a pressure that is normal to the surface. Since the FSI models are transient, the TVPM and LVPM forces are now functions of time. According to EMG data found in literature [18], the muscle wave forms can be approximated as shown below in Figure 26.

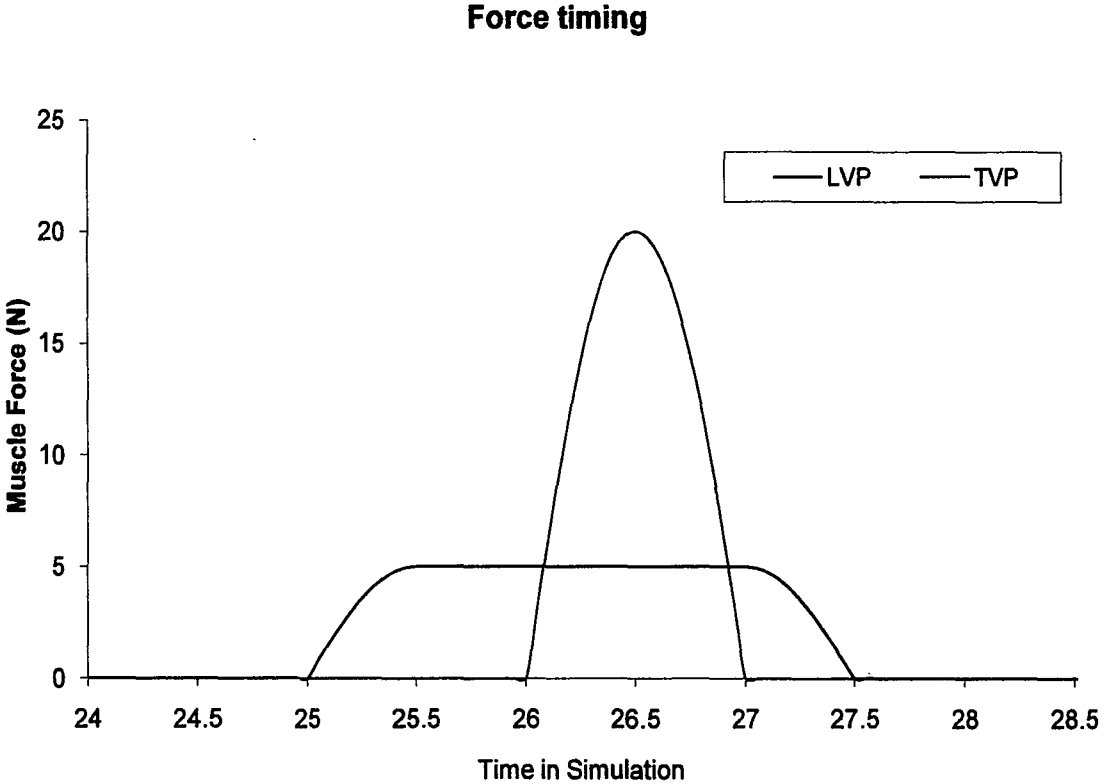


**Figure 26: Muscle Force Waveforms in Simulation**

The LVPM force ramps up as a quarter sine wave over 0.5 sec, holds constant for 1.5 sec, then ramps down as a quarter sine wave over 0.5 sec. The TVPM force is a half sine wave with a duration of 1 sec.

In the fluid domain, the working fluid is air and the flow is governed by the incompressible, continuity and Navier-Stokes equation

$$\rho\frac{\partial v_i}{\partial x_i} = 0 \; and \; \rho\frac{\partial v_i}{\partial t} + \rho v_i\frac{\partial v_j}{\partial x_i} = -\frac{\partial p}{\partial x_i} + \mu\frac{\partial^2 v_i}{\partial x_i x_j} \qquad (21)$$

where $\rho$ is the density of air, 1.229 kg/m$^3$, $\mu$ is the viscosity of air, 1.8x10$^{-5}$ Pa·s, and $v$ is the velocity vector. Since the FSI models are made to replicate clinical tests, a normal traction is applied to the ME (least distal) end of the lumen and a zero pressure boundary

condition is applied to the NP (most distal) end of the lumen to establish a baseline flowrate. The other sides of the lumen are identified as FSI interfaces and have the corresponding boundary conditions applied, which are described below.

For the FEA model to truly be a FSI model, then coupling between the solid and fluid domains needs to exist. In ADINA, the coupling between the domains is achieved by solving the equations for one domain, then solving the equations in the other domain and iteratively going back and forth until convergence is reached. Between the domains, there are three boundary conditions that are enforced. First, a kinematic condition requiring displacement continuity is imposed.

$$d_i^f = d_i^s \tag{22}$$

The second condition requires velocity continuity between the domains.

$$n_i^f v_i = n_i^s \frac{\partial d_i^s}{\partial t} \tag{23}$$

It states that the normal velocity in the fluid domain on the interface must be equal to the normal velocity of solid on the interface. The third boundary condition is a dynamic condition that requires stress continuity between the domains.

$$n_i^f \sigma_{ij}^f = n_i^s \sigma_{ij}^s \tag{24}$$

Figure 27 shows a plot containing velocity vectors at different time steps in the simulations when the muscles are acting on the ET.

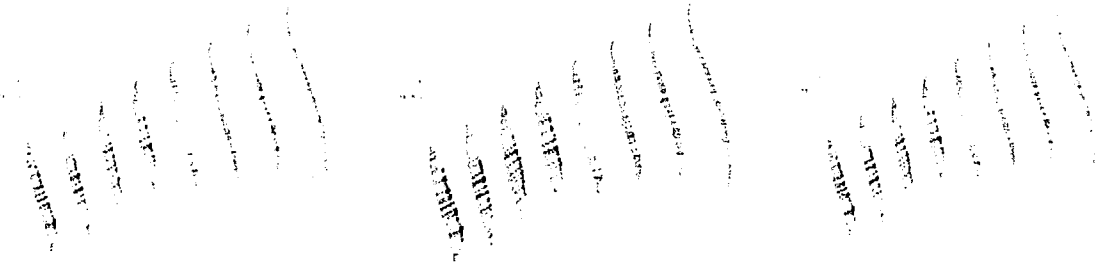


**Figure 27: Velocity plot at different time steps in the simulation**

Just like in Chapter II, once the flow field has been solved for, the velocity profile at the mid cross section of the lumen is integrated at every time step to find the flowrate and then a resistance parameter is calculated by

$$R_v(t) = \frac{\Delta P}{Q(t)} \tag{25}$$

This resistance parameter is calculated to facilitate comparison of the numerical data with experimental data. Since the models are transient, Q=Q(t) so the resistance can then be found as a function of time and plotted just like in Figure 5.

Finally, since these are transient models, some thought had to go into deciding on a reasonable time step for the model to make computation as efficient as possible while yielding good results. The model goes through four distinct time regions during one simulation. Looking at Figure 26, the first zone from time=0 sec up until time=12.5 sec, the pressure in the fluid domain is ramping up linearly from 0 mm $H_2O$ up to 200 mm $H_2O$. Then from time=12.5 sec up to time=25 sec, the model is equilibrating, letting any of the viscoelastic effects from the pressure ramp up decay away before the muscle activity starts. Then from time=25 sec until time time=27.5 sec is when all the muscle activity takes place as described in Figure 26. Then from time=27.5 sec until the

simulation ends at time=30 sec the model is again allowed to equilibrate. Ideally, you would like to take small time steps when the fluid pressure is ramping up, take large time steps when the model is equilibrating, and then take very small time steps when the model is undergoing muscle activity. However, it was found that changing the time step multiple times during a simulation led to numerical instabilities in the solver and as a result the solution would not converge. So the decision was made to fix the time step at a reasonable value for stability. The time step of 0.1 sec was chose because it could easily resolve all the muscle activity and give a reasonable value of 300 time steps for a simulation. Then, to validate this choice, one simulation was run at a time step of 0.05 sec to compare the results.

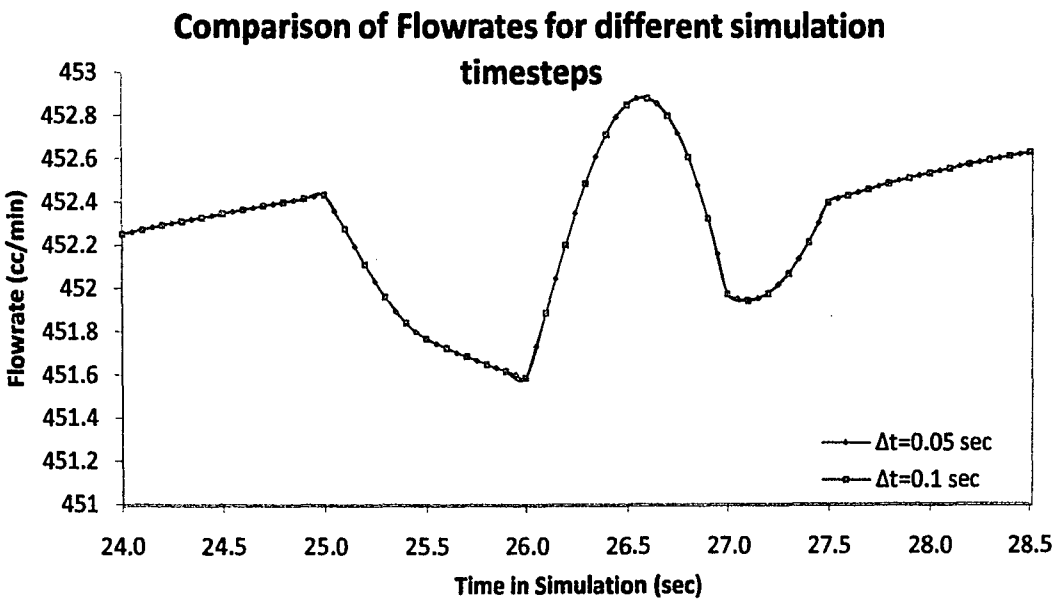


**Figure 28: Comparison of results for different simulation time steps**

As Figure 28 shows, cutting the time step in half produces exactly the same results. This validates our choice of $\Delta t$=0.1 sec, therefore all simulations were then run with a $\Delta t$=0.1 sec.

## B. Muscle Delay Timing Study

For this study, relative muscle timing was changed to see what influence it would have on ET function when comparing the healthy adult to the cleft palate patient. The parameter that was varied is $t_d$, as defined in Figure 29. Note that in the below figure, $t_d$ is equal to 1 sec.

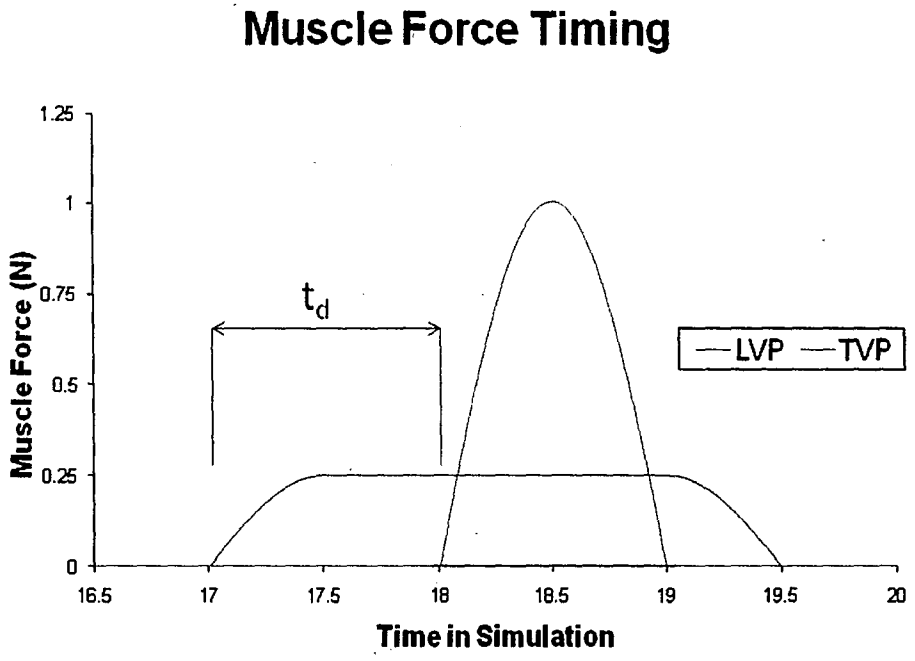


**Figure 29: Definition of Delay Time for Study**

Physically, when $t_d$is negative or larger than the duration of the LVPM, the TVPM acts independently of the LVPM. When $t_d$is in the middle of the range, the TVPM and LVPM act together. The parameter $t_d$was varied through the range -1.0 sec up to 2.5 sec with data points taken at an interval of 0.25 sec. Simulations were run at $t_d$= -1.0 sec, -0.75 sec, -0.5 sec, all the way up to $t_d$= 2.0 sec, 2.25 sec, 2.5 sec.

## C. Results

### i. Results matching Forced Response Test

Experimental results from Forced Response Tests all have the same general shape as seen below in Figure 30.

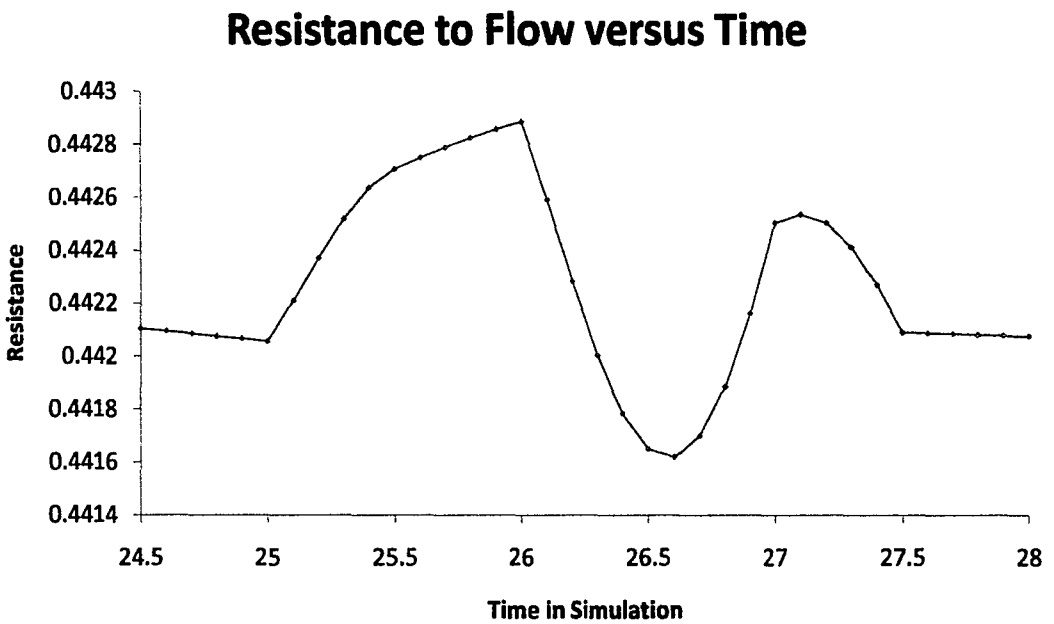


**Figure 30: Typical resistance plot showing different regions**

In the above figure, from time=25 sec until time=26 sec, there is an increase in $R_v$, this is known as a pre-swallow constriction and is mainly due to LVPM contraction. Then from time=26 sec to time=27 sec, there is a sharp drop and rise of $R_v$, this region is known swallow dilation and is mainly due to TVPM contraction. Finally from time=27 sec to time=27.5 sec, this region is known as post-swallow constriction and is mainly due to continued LVPM contraction. You can see all three of regions in all the experimental data, such as Figure 5. On the vertical axis of Figure 30, one can see that the resistance values change very little, 0.5% - 1% while in Figure 5 the resistance values change significantly, 75% - 100%. This is due to a meshing constraint within ADINA. ADINA

can only use first order fluid elements, so as a result many elements are needed to discretize the fluid domain and produce accurate results. Shown in Figure 31 is the

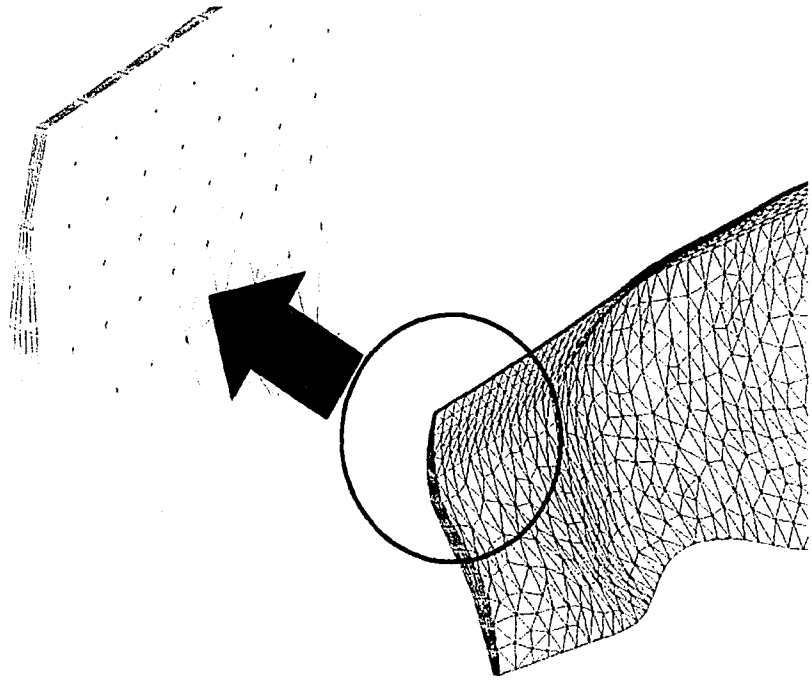

**Figure 31: ADINA fluid domain mesh**

mesh used in the fluid domain for all the simulations. Notice that seven elements are needed across the lumen to get good results. The problem with using this mesh for the ET is that when the ET opens or closes, the lumen goes through very large deformations, on the order of 150% increase in volume, or a cross sectional aspect ratio (width of opening/height of opening) change from 100:1 down to 5:1. The large deformations cause the very small elements to collapse onto themselves which fails the simulation. The sliver tetrahedron that are present across the opening of the lumen deform so much that a tetrahedron will get turned inside-out or degrade far enough that it has an interior angle of greater than 120° therefore making the element invalid. Therefore, all models need to be run with forces that are an order of magnitude lower than the prescribed physiological forces. As a result, the change in flow resistance calculated by the FSI

models are significantly smaller than the changes measured experimentally. This problem is addressed more in Chapter IV when new techniques are developed to solve this problem.

### ii. Results matching Modified Forced Response Test

As talked about in Chapter I, performing a Modified Forced Response test in the clinic involves generating hysteresis loops in pressure and flow rate to help find mechanical properties of the tissue. Since the FSI models created are transient, the boundary conditions in the FSI models can be set to replicate this clinical test. Using this clinical test is a very good way of validating the material properties of the FSI model. Shown in Figure 32 is a comparison of a hysteresis loop obtained from a healthy adult model and the results from the corresponding FSI model.

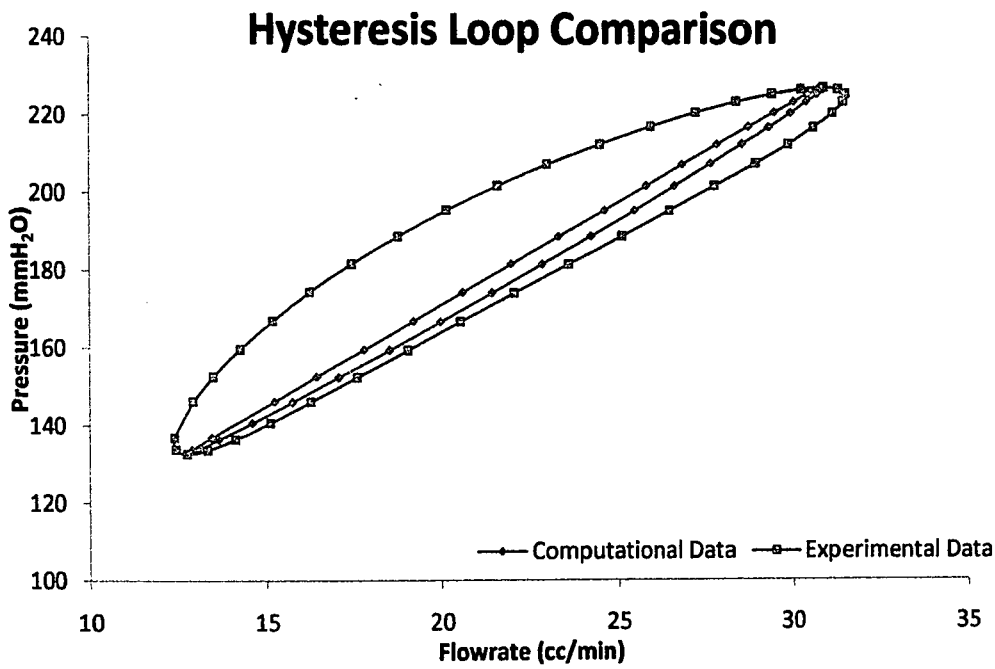


**Figure 32: Healthy adult hysteresis loop comparison**

Figure 32 shows that the computational model is in fairly good agreement with the experimental test. The slope of the hysteresis loop appears to match, but the

experimental model has more viscoelastic effects as given by more area in the loop. However, we could not get the simulations to match the viscoelastic aspects of the experimental data due to problems with the model. The hysteresis loop in Figure 32 was obtained with the baseline material parameters used in the FSI models. The problem with the model is that going back and changing the material properties then rerunning the simulation has extremely minimal effect on the hysteresis loop. This problem has two major sources. First, during the clinical test, the ET is open very little. To create an FSI model, we used 200 mm $H_2O$ of pressure to create an open model as described in the Methodology section in this chapter. However, using 200 mm $H_2O$ might have made too large an ET opening. However, using 100 mm $H_2O$ of pressure to create an open lumen exacerbated the meshing constraints as described in the above Forced Response Matching Results section. Secondly, the boundary conditions may not be exactly correct to get the best results. Again, as stated in the Methodology section in this chapter, we use a zero pressure boundary condition on the downstream end of the ET.

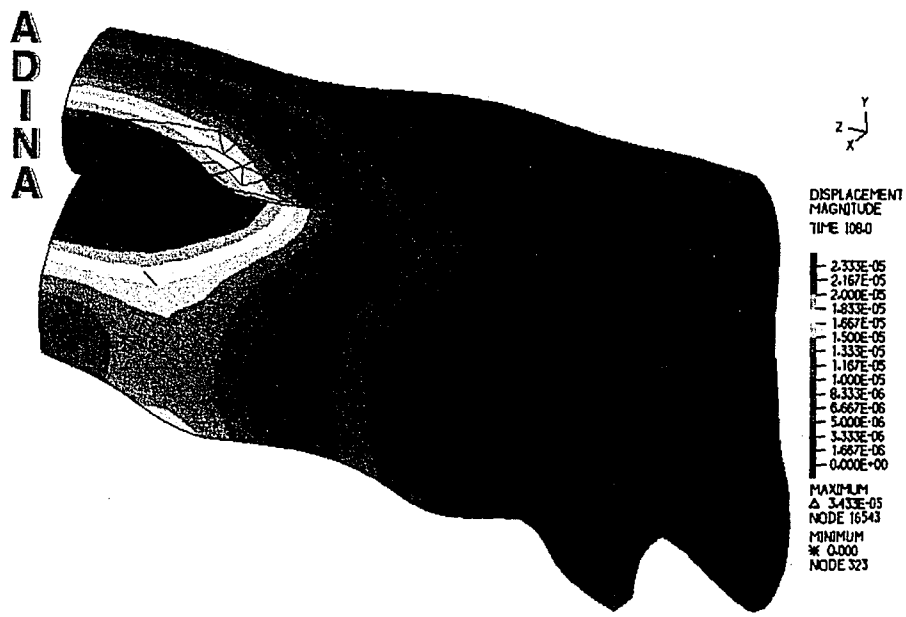


**Figure 33: Displacement magnitude plot from a Modified Forced Response Simulation**

viscoelastic model has more viscoelastic effects as given by more area in the loop. However, we could not get the simulations to match the viscoelastic aspects of the experimental data due to problems with the model. The hysteresis loop in Figure 32 was obtained with the baseline material parameters used in the PSI models. The problem with the models is that going back and changing the material properties then rerunning the simulation has extremely minimal effect on the hysteresis loop. This problem has two probable causes. First, during the clinical test, the LV is open very little. To create an PSI model we used 200 mm Hg of pressure to create an open model as described in the Model Settings section in this chapter. However using 200 mm Hg might have made too long of a opening. However, using 100 mm Hg of pressure to create an open lumen created the meshing constraints as described in the above Forced Response Matching section. Secondly, the boundary conditions may not be exactly correct to get the best results. Again, as stated in the Methodology section in this chapter, we use a zero pressure boundary condition on the downstream end of the LV.

Figure 33: Displacement magnitude plot from a Modified Forced Response Simulation

As a result (shown in Figure 33), in the solid model there is no displacement and no stress in the tissues near the NP end (least distal) of the ET implying that not all the tissue is being engaged by the pulsatile pressure like in the clinical test. The simulations will not give good results until all the tissue is engaged which might be able to be accomplished by changing the boundary conditions. Right now, we impose a 200 mm $H_2O$ pressure drop between the ME and the NP buy using 200 mm $H_2O$ at the ME and 0 mm $H_2O$ at the NP because 200 mm $H_2O$ is externally applied in the clinical test and the pressure is assumed to be 0 mm $H_2O$ in the NP. However, it might be possible to better replicate clinical test results using 300 mm $H_2O$ at the ME and 100 mm $H_2O$ at the NP. Doing this should help to engage all the tissue thus producing better results.

### iii. Muscle Timing Study

The previous two results sections serve as qualitative model verification. Although the current model does not match of experimental magnitudes perfectly, it does reproduce experimentally perceived trends. Given this state of the model, it is verified enough to do a comparative study. For this study, the goal is to find out how muscle timing affects ET function in a healthy adult and a cleft palate infant. For each simulation, a specific $t_d$ was chosen and then a Forced Response Test was simulated. So a total of 30 simulations were run to compile the data shown below. For this study, two pieces of data were extracted from each simulation, the magnitude of pre-swallow constriction and the magnitude of the swallow dilation. Figure 34 is a plot of the flowrate of air through the ET from a simulation. The two quantities measured in this study are shown on the graph.

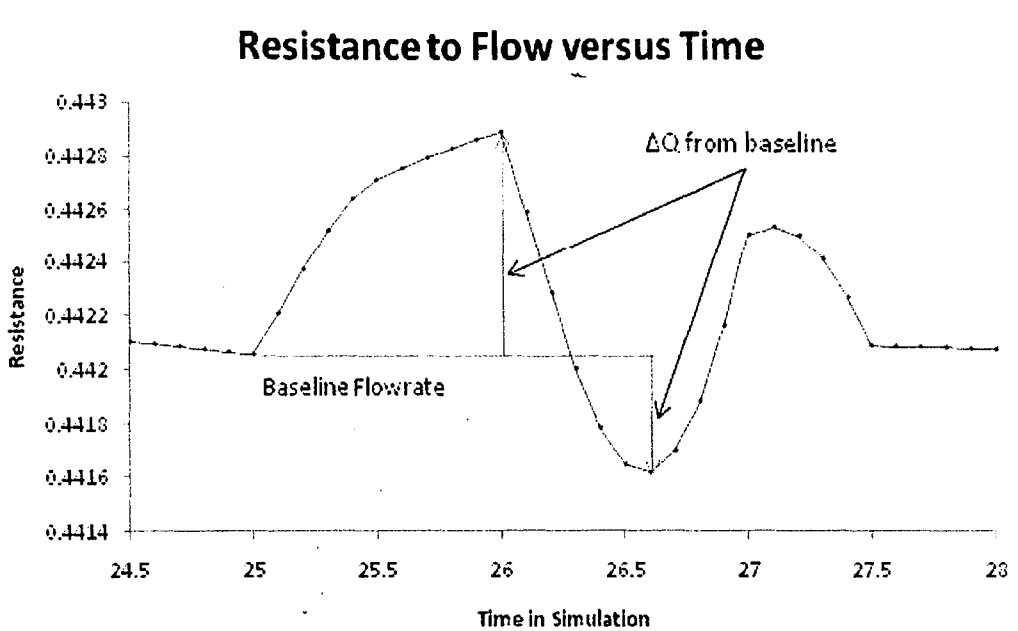


**Figure 34: Definition of quantities in Muscle Timing Study**

All the results presented below in a new parameter called the sensitivity, which is calculated differently from the sensitivity in Chapter II. This sensitivity parameter is best described as a slope. To calculate the parameter, $t_d = 0$ was taken as the baseline. The sensitivity parameter is then defined as

$$\frac{R_v|_{t_d=yy} - R_v|_{t_d=0}}{yy - 0} \tag{26}$$

where yy can take on any of the $t_d$ values, except 0 sec. During this study, sensitivities were calculated with $t_d = -1, t_d = 1, t_d = 2, t_d = 2.5$.

All the results from the study are summarized in the following two graph and two tables.

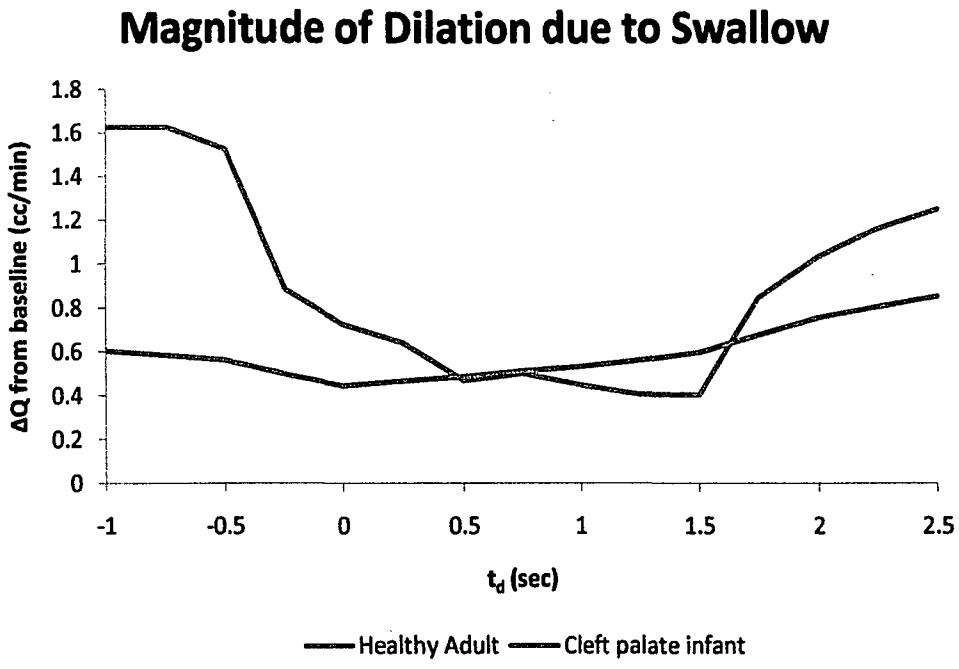


**Figure 35: Magnitude of Lumen Dilation**

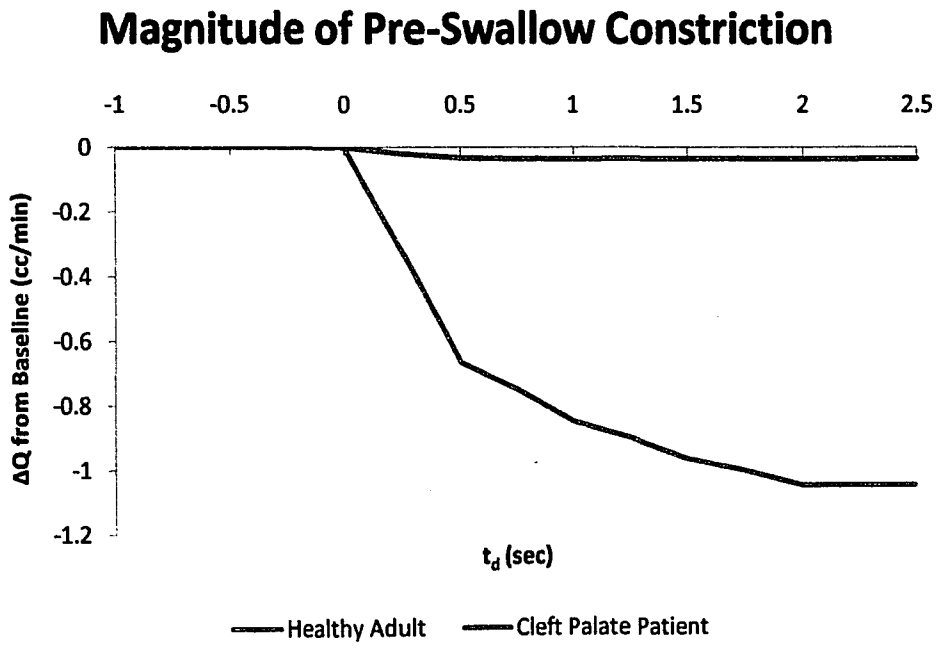


**Figure 36: Magnitude of Pre-Swallow Constriction**

On the vertical axes of both of the graphs is ΔQ from baseline as defined in Figure 34. Looking at Figure 35, you will see that the lumen dilation is largest in healthy adults when the TVPM is acting independently of the LVPM (i.e. $t_d$ is negative or very large). Looking at Figure 36, as you would expect, when $t_d$ is less than 0 sec, there is no pre-swallow constriction since the TVPM is acting before the LVPM. In both figures, you will notice that the line corresponding to the cleft palate patients is very flat compared to the healthy adult line.

**Table 4: Sensitivity of Swallow Dilation**

| Sensitivity of Swallow Dilation | | |
|---|---|---|
| Sensitivity Value | Cleft Palate | Healthy Adult |
| $Sensitivity_{0\rightarrow -1}$ | 0.16 | 0.9018 |
| $Sensitivity_{0\rightarrow 1}$ | 0.0864 | 0.276 |
| $Sensitivity_{0\rightarrow 2}$ | 0.1563 | 0.1563 |
| $Sensitivity_{0\rightarrow 2.5}$ | 0.1632 | 0.3921 |
| Averages | 0.141475 | 0.43155 |

**Table 5: Sensitivity of Pre-swallow Constriction**

| Sensitivity of Pre-Swallow Constriction | | |
|---|---|---|
| Sensitivity Value | Cleft Palate | Healthy Adult |
| $Sensitivity_{0\rightarrow 1}$ | 0.0354 | 0.846 |
| $Sensitivity_{0\rightarrow 2}$ | 0.0177 | 0.5241 |
| $Sensitivity_{0\rightarrow 2.5}$ | 0.0064 | 0.4193 |
| Averages | 0.019833 | 0.59646 |

For these sensitivity values, the higher the sensitivity value, the more of a change in ET function is recorded. All the values in Table 4 and Table 5 reinforce the results from the graphs. The adult sensitivities for both pre-swallow constriction and swallow dilation are both much higher than the respective values for the cleft palate patient. This fact leads to the biggest conclusion drawn from this study, cleft palate patients are insensitive to muscle timing. This is not a big surprise given the cleft palate insensitivity to muscle forces as found in Chapter II. In this study, the only difference in the models is the

morphology; muscle forces, tissue stiffness, and muscle timing are all the same. This reinforces the hypothesis that morphology is the underlying factor in ET dysfunction and changing muscle timing is not a viable option for treatment in this patient group.

## D. Discussion

As previously stated, it is imperative that we understand the mechanisms of ET dysfunction if we want to be able to treat diseases such as chronic OM. In this chapter, fully coupled FSI models were created to capture the transient phenomena that occur during ET closing and opening. The models created were capable of reproducing experimental trends so they were then used for a parametric study. This study included one healthy adult patient and one cleft palate infant, and the parameter being investigated was muscle delay timing. It was found that the cleft palate patient was insensitive to muscle timing changes. Sensitivity values for the cleft palate patient were on the order of 0.14 and 0.019 respectively for swallow dilation and pre-swallow constriction while the values for the healthy adult were 0.431 and 0.596 respectively for swallow dilation and pre-swallow constriction. These values lead to the conclusion that the cleft palate patient is insensitive to muscle timing changes and that therefore, changing the muscle timing in these patients in not a viable option for treating ET dysfunction. This reinforces the original hypothesis that only surgically correcting the morphology will lead to better ET function.

# IV. Advanced Finite Element Techniques

## A. Modeling the Middle Ear (ME)

Some efforts have been made into modeling the auditory canal, tympanic membrane and Middle Ear (ME). During the clinical tests, the tympanic membrane is punctured and the entire system from the edge of the auditory canal through the ME is inflated with pressure. This allows the volume inside the middle ear to potentially act as a pressure reservoir, supplying air flow through the ET. A literature search revealed that the average volume of the ME in healthy adults was 0.5 $cc^3$ [19]. Using this information, a very rough CAD model of the auditory canal, tympanic membrane and the ME was made as shown in Figure 37.

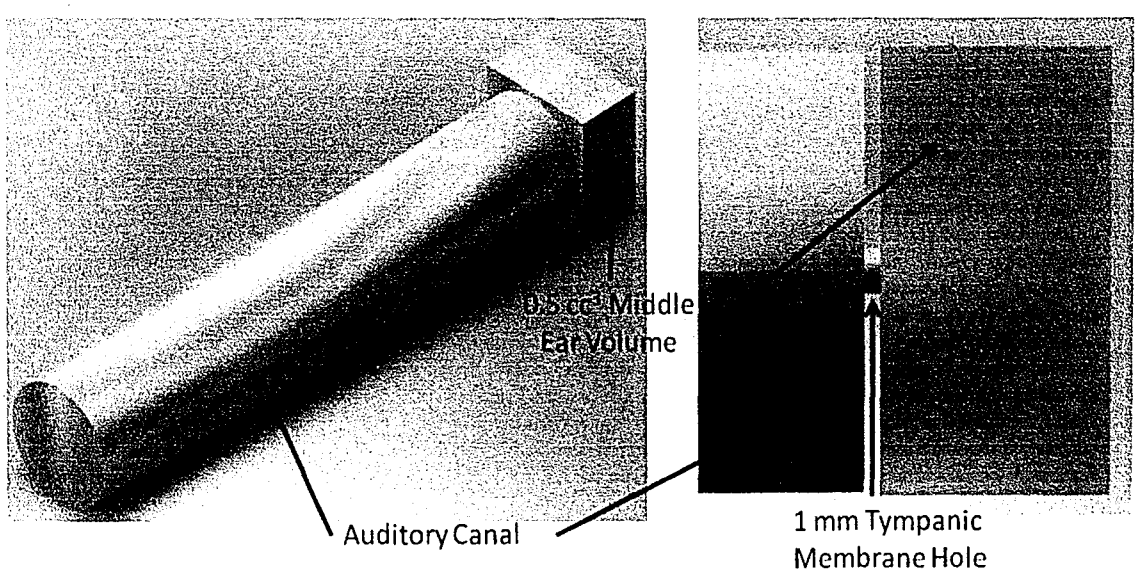


**Figure 37: CAD model of auditory canal, Tympanic membrane, and ME**

The auditory canal is represented by a cylinder, then a round 1 mm diameter hole in the tympanic membrane and a box with the anatomically correct volume of 0.5 $cc^3$ to represent the ME. This model was then incorporated into some of the FEM models to see

# IV. Advanced Finite Element Techniques

## A. Modeling the Middle Ear (ME)

Some efforts have been made into modeling the auditory canal, tympanic membrane and Middle Ear (ME). During the clinical tests, the tympanic membrane is punctured and the entire system from the edge of the auditory canal through the ME is inflated with pressure. This allows the volume inside the middle ear to potentially act as a pressure reservoir, supplying air flow through the ET. A literature search revealed that the average volume of the ME in healthy adults was 0.5 $cc^3$ [19]. Using this information, a very rough CAD model of the auditory canal, tympanic membrane and the ME was made as shown in Figure 37.

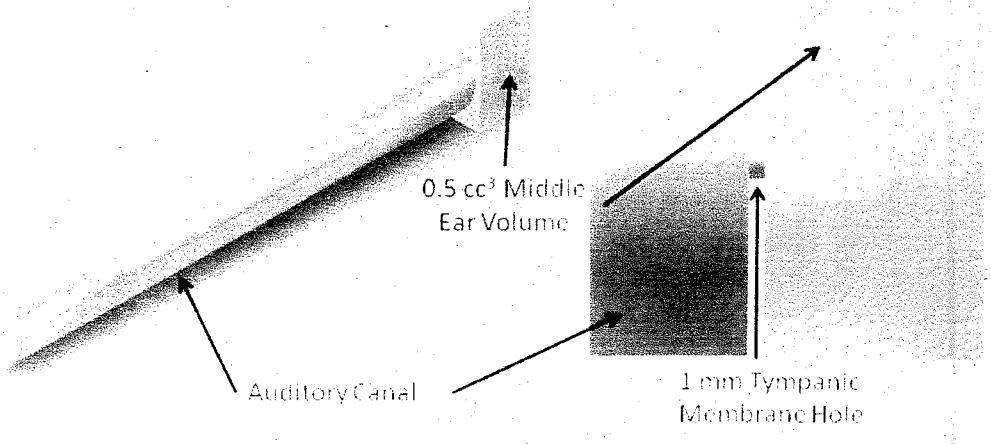


**Figure 37: CAD model of auditory canal, Tympanic membrane, and ME**

The auditory canal is represented by a cylinder, then a round 1 mm diameter hole in the tympanic membrane and a box with the anatomically correct volume of 0.5 $cc^3$ to represent the ME. This model was then incorporated into some of the FEM models to see

what result it would have. It was inserted into a Modified Forced Response Test model as shown in Figure 38.

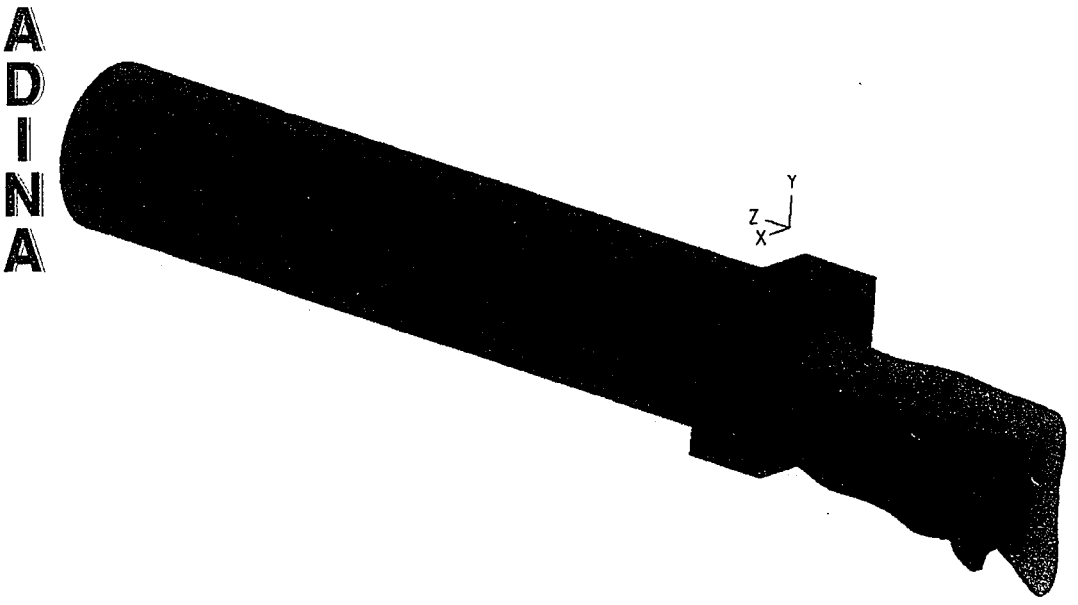


**Figure 38: FEA model including the Middle Ear Model**

Figure 38 shows the scale difference of the ET problem. The ME is relatively large when compared to the ET. For this model, the externally applied pressure was then applied to the end of the auditory canal. Unfortunately, inserting the ME model had a minimal effect on the overall results of the simulation. As mentioned in Chapter II, Section C, ii, it is hypothesized that one of the problems with the model is the fact that the starting lumen opening is too large. One result of this problem is large flowrates and therefore small resistances when compared to the experimental data. Putting the ME model in the simulation alleviated this problem slightly. The flowrates through the lumen were effectively cut in half, so the resistances got larger, but were still much smaller than the experiments. Modeling the ME to match clinical tests proved to have little effect now, however the model of the ME is going to be very important in future problems, such as simulating the drainage of ME mucus through the ET.

## B. Large Deformation Modeling

Due to the large displacements seen during the opening and closing of the ET, ADINA is not a suitable program for performing the analysis. Once this was realized, a search began for a method that would be able to handle such large displacements. The solution was found in a different FEA program called COMSOL.

The difference in the method goes all the way back to the very fundamentals of the finite element procedure. Once the geometry is meshed, basis functions must be chosen to interpolate the unknown quantities across the elements. When performing CFD, the unknown quantities, or Degrees of Freedom (DOF), are x-velocity, y-velocity, z-velocity, and pressure. ADINA can only support basis functions that are first order, meaning that only linear changes of the DOFs are allowed across any given element. With something as complicated a fluid flow, this means that many elements are required to capture the flow field. COMSOL can use elements that have much higher order basis functions. To solve this specific mesh collapsing problem, elements with 4th order basis functions are implemented. This means that now the DOFs can vary as a 4th order polynomial across any given element. With 4th order elements, the element itself can be much larger so fewer are required to capture the flow field with the same accuracy as first order elements.

This method difference can easily be verified. In Ghadiali *et al.* [8], an analytical solution is derived for pressure driven flow through a spinal needle that is 0.3 mm in diameter and 8 cm in length. The analytical solution gives the following relationship between pressure difference and flowrate through the needle.

$$\Delta P = \frac{\mu L Q}{A^2}\Gamma \tag{27}$$

where $\Delta P$ is the pressure drop across the length of the needle, L is the length of the needle, A is the cross sectional area of the needle, $\mu$ is the viscosity of the working fluid, and $\Gamma$ is a hydraulic shape factor based only on the geometry. Using air as the working fluid, a 200 mm $H_2O$ pressure drop through the needle, L=8 cm, $A=\pi R^2$ for a circle, and $\Gamma=8\pi$ for a circle, the flowrate Q can be found to be $2.703e^{-7}$ $m^3/s$. Then the spinal needle is modeled in both ADINA and COMSOL with their corresponding meshes. The differences in the mesh are outlined in Figure 39.

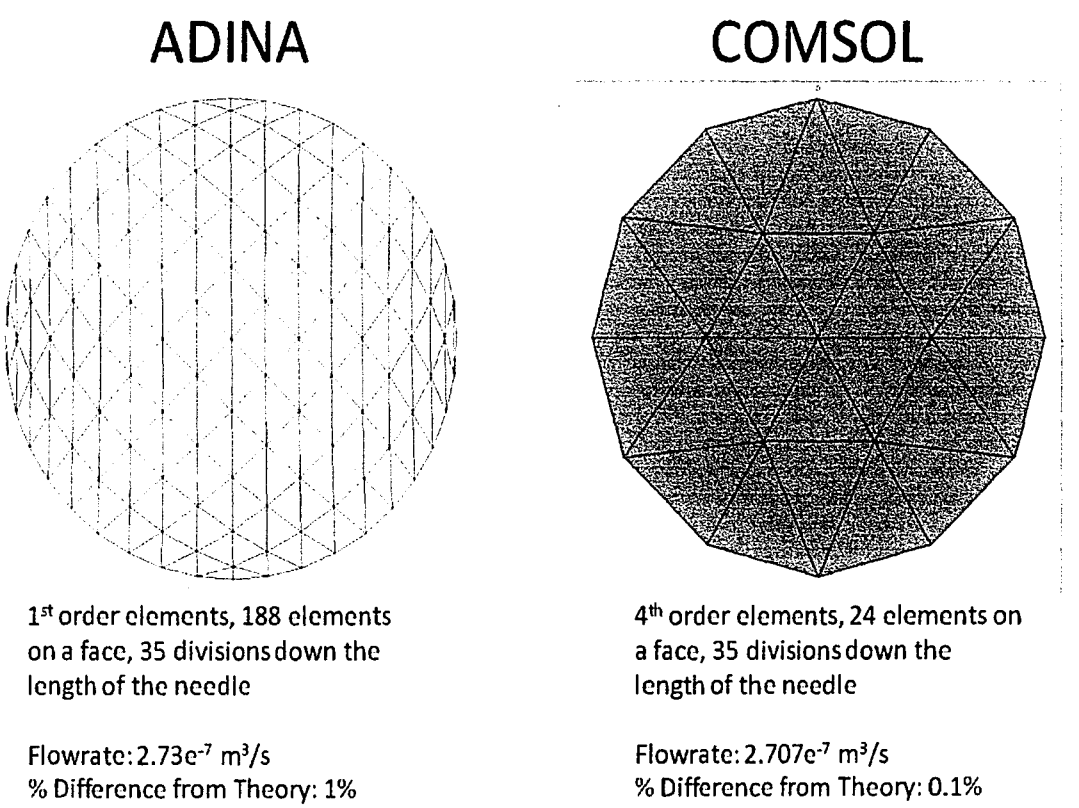


**Figure 39: Comparison of the mesh used in both system verification models**

As seen in the figure above, the ADINA model used 188 elements on a face with 35 divisions down the length of the needle giving a total of 6580 1st order elements resulting in a 1% difference with its calculated flowrate as compared to the theoretical value.

where $\Delta P$ is the pressure drop across the length of the needle, L is the length of the needle, A is the cross sectional area of the needle, $\mu$ is the viscosity of the working fluid, and $\Gamma$ is a hydraulic shape factor based only on the geometry. Using air as the working fluid, a 200 mm $H_2O$ pressure drop through the needle, L=8 cm, $A=\pi R^2$ for a circle, and $\Gamma=8\pi$ for a circle, the flowrate Q can be found to be $2.703e^{-7}$ $m^3/s$. Then the spinal needle is modeled in both ADINA and COMSOL with their corresponding meshes. The differences in the mesh are outlined in Figure 39.

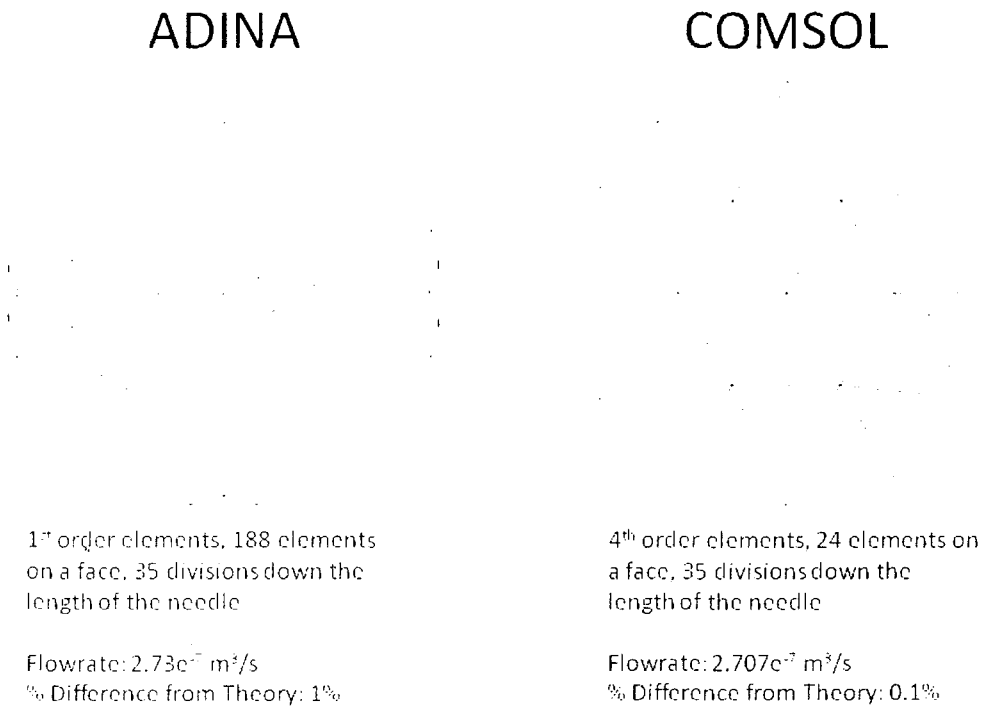


**Figure 39: Comparison of the mesh used in both system verification models**

As seen in the figure above, the ADINA model used 188 elements on a face with 35 divisions down the length of the needle giving a total of 6580 1st order elements resulting in a 1% difference with its calculated flowrate as compared to the theoretical value.

COMSOL used only 24 4th order elements on a face with 35 divisions down the length of the needle for a total of 840 4th order elements resulting in a 0.1% difference with its calculated flowrate as compared to the theoretical value. Note that in Figure 39, the COMSOL mesh plot shows linear elements. The elements are truly 4th order as basis functions, and also 4th order in shape as well, however COMSOL has no way of visualizing higher order elements. This verifies that 4th order elements can be just as accurate as 1st order elements even though they are much bigger.

Applying this new method to the ET problem yields very good results. Using 4th order elements allow us to use very few elements across the lumen opening thus allowing for much larger displacements. Pictured below is a test model that demonstrates this new method.

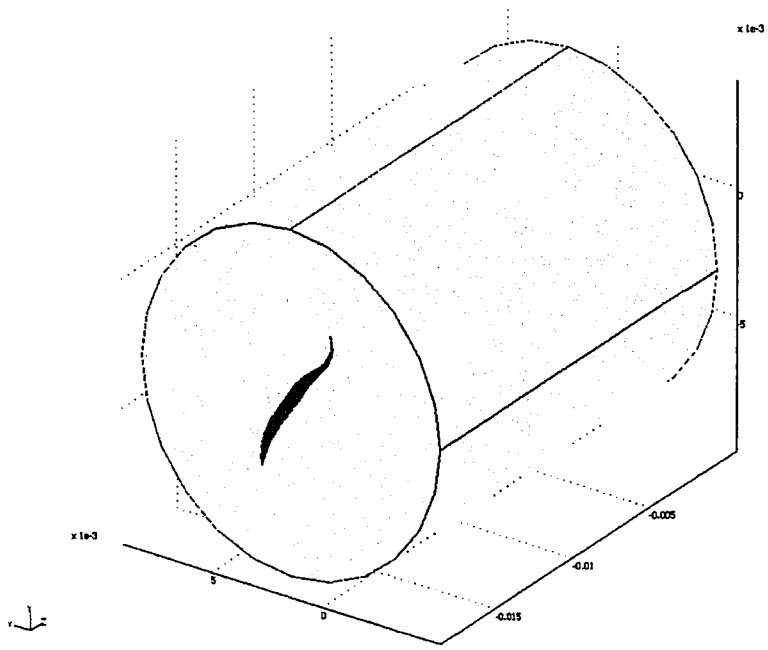


**Figure 40: Test model in COMSOL using new method**

In this new test model, there is an anatomically correct lumen opening surrounded by a cylinder of cartilage. This a fully coupled FSI model to demonstrate how using a mesh

with mixed elements types work. The cylinder is meshed with 2nd order tetrahedral solid elements while the fluid domain is meshed with 4th order tetrahedral fluid elements and the domains are coupled using an Arbitrary Lagrangian Eulerian (ALE) method.

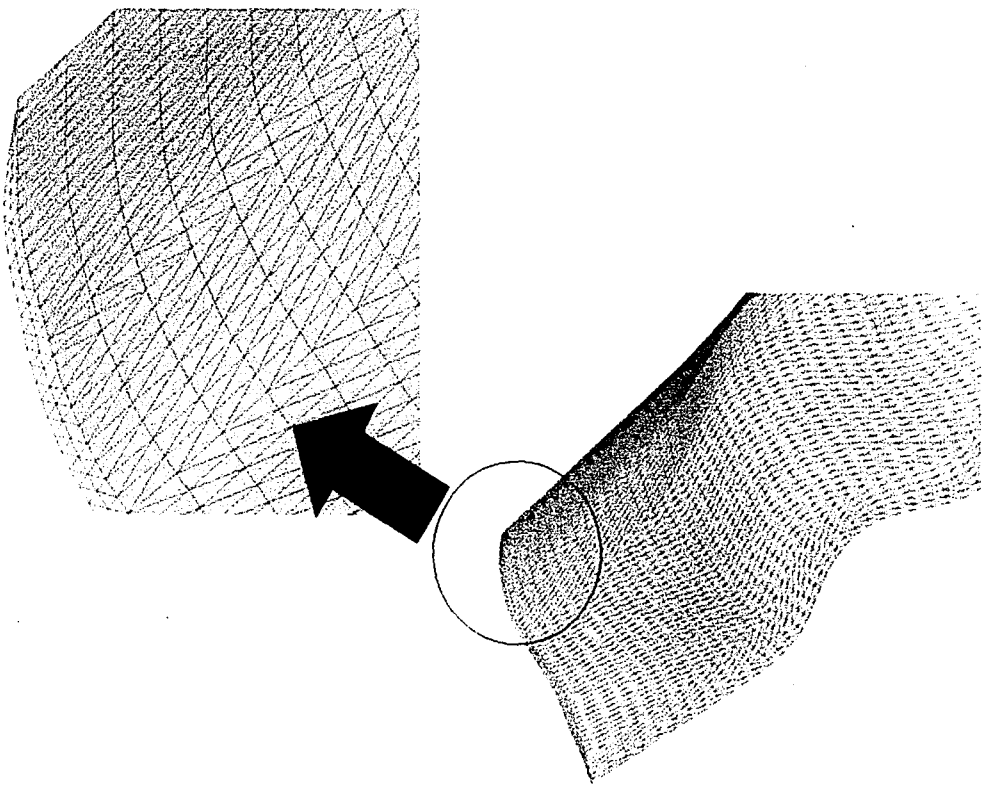

**Figure 41: Mesh in the COMSOL fluid domain**

As you can see in Figure 41, the mesh of 4th order elements is much coarser than the mesh of 1st order elements used in Figure 31. In COMSOL, only two elements across the lumen opening are needed. Having these large tetrahedral allows for much more deformation without any element collapse.

In this model the cartilage is represented by a hyper-elastic Mooney-Rivlin material model just as in ADINA. The material model is formulated the same way as described in Chapter II, Methodology, equations (1) - (4). In the fluid domain, the flow is governed by the incompressible continuity and Navier-Stokes equation just as described in Chapter III, Methodology, equation (21). The major difference between ADINA and

with mixed elements types work. The cylinder is meshed with 2nd order tetrahedral solid elements while the fluid domain is meshed with 4th order tetrahedral fluid elements and the domains are coupled using an Arbitrary Lagrangian Eulerian (ALE) method.

**Figure 41: Mesh in the COMSOL fluid domain**

As you can see in Figure 41, the mesh of 4th order elements is much coarser than the mesh of 1st order elements used in Figure 31. In COMSOL, only two elements across the lumen opening are needed. Having these large tetrahedral allows for much more deformation without any element collapse.

In this model the cartilage is represented by a hyper-elastic Mooney-Rivlin material model just as in ADINA. The material model is formulated the same way as described in Chapter II, Methodology, equations (1) - (4). In the fluid domain, the flow is governed by the incompressible continuity and Navier-Stokes equation just as described in Chapter III, Methodology, equation (21). The major difference between ADINA and

COMSOL is in how the FSI coupling is done. As stated before, ADINA solves the fluid domain, then solves the solid domain and iterates back and forth between the domains until convergence is reached. In COMSOL, an ALE method is used which introduces more DOFs into the model, but then, in this case, solve the fluid equations in the moving frame of reference as defined by the ALE method. In the ALE method, let the fixed spatial coordinates be X, Y, Z and let the moving coordinate system be defined as x, y, z. x, y, and z are new variables introduced into the model that must be solved for. So at the beginning of the problem, X and x are the same, Y and y are the same, and Z and z are the same. The equations for the ALE displacements are as follows.

$$\frac{\partial^2}{\partial X^2}\frac{\partial x}{\partial t}+\frac{\partial^2}{\partial Y^2}\frac{\partial x}{\partial t}+\frac{\partial^2}{\partial Z^2}\frac{\partial x}{\partial t}=0 \tag{28}$$

$$\frac{\partial^2}{\partial X^2}\frac{\partial y}{\partial t}+\frac{\partial^2}{\partial Y^2}\frac{\partial y}{\partial t}+\frac{\partial^2}{\partial Z^2}\frac{\partial y}{\partial t}=0 \tag{29}$$

$$\frac{\partial^2}{\partial X^2}\frac{\partial z}{\partial t}+\frac{\partial^2}{\partial Y^2}\frac{\partial z}{\partial t}+\frac{\partial^2}{\partial Z^2}\frac{\partial z}{\partial t}=0 \tag{30}$$

Now, all the equations for the solid domain written in the fixed reference frame, the ALE equations, and the equations for the fluid domain written in the moving reference frame are all assembled into one system and solved simultaneously.

Results from this test model are very promising. Figure 42 is shows a snapshot of the deformed model as well as fluid streamlines at a given point during the simulation.

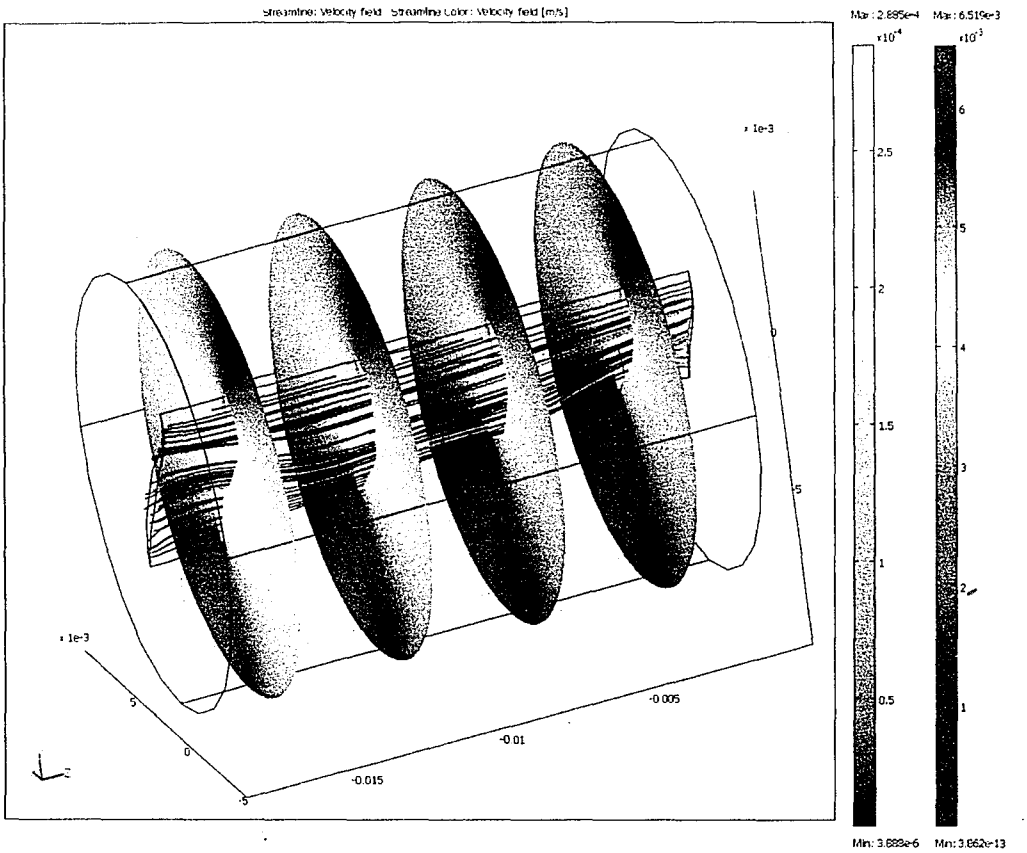


**Figure 42: Deformed COMSOL test model**

The most important thing to note about this model is the scale of the deformation. The original lumen opening is roughly 2 mm tall and 0.1 mm wide then undergoes displacements on the order of 0.3 mm, and strains of greater than 10 %. Comparing the volume of the lumen opening of the un-deformed model to that of the deformed model shows the opening underwent a 262% increase in lumen volume without element collapse.

# V. Conclusions and Future Work

In Chapter II, decoupled FEA models were created so that a parameter variation study could be conducted in both a healthy adult patient and in cleft palate patients. The parameter variation study in the healthy adult showed that ET function is most sensitive to TVPM force magnitude and the modulus of elasticity of the glandular tissue, changing these two parameters made the biggest difference in how well the ET performed. This conclusion is based on the sensitivity values in Table 2. The only parameters with a high impact sensitivity values were the TVPM magnitude, 5.516 and the $E_{Gland}$, 0.217. All the other parameters had sensitivity values that were close to 1 meaning that changes in these parameters had little to no effect on ET function. The sensitivity value for the TVPM being much greater than 1 implies that increasing the TVPM force improves ET function, and the sensitivity value for the glandular tissue being much smaller than 1 implies that decreasing the tissue stiffness improves ET function. Using this information, a parameter variation study was done in six cleft palate patients where the TVPM and LVPM force magnitude was varied to study its respective impact when the morphology is altered. It was found that most patients showed little sensitivity to the TVPM force, however there was an outlier patient that showed extreme sensitivity but this due mainly to the highly altered morphology and size difference compared to the other patients. Both the TVPM and LVPM magnitudes had very low average sensitivity values, 1.46 and 1.00 respectively. These results reinforce that hypothesis that the morphology is the underlying cause for poor ET function. Studying the results of the most current studies and previous studies done in our lab [6-9] suggest that the only way to improve ET

function in pathological patients with a cranio-facial disease, such as a cleft palate, is to surgically alter ET morphology. This can be accomplished at the same time when the surgeon is repairing the hard palate.

Then in Chapter III, fully coupled FSI models of the ET were created to better replicate two clinical tests and to capture the complex ET opening and closing phenomena observed experimentally. The FSI models created were able to both qualitatively and quantitatively replicate experimental trends with some limitations. The models were then used to perform a parameter variation study where relative TVPM and LVPM timing was varied to see its effect on ET function. It was shown that the cleft palate patient showed very little sensitivity to muscle timing compared to the healthy adult patient. As showed in Table 4 and
Table 5, the sensitivity values of the cleft palate patient is significantly lower than the sensitivity values of the healthy adult. This is not a surprising result given the results from Chapter II showing that changes in the TVPM and LVPM muscle forces had little effect on ET function. Again, this reinforces the hypothesis that altering the morphology is the only way to restore ET function.

Then in Chapter IV new techniques were developed to model more of the complicated ET system. A model was developed that connected the ME with the ET and will be used in the near future to create FSI models that simulate gas exchange dynamics and the drainage of highly viscous ME fluid via the ET. Then, a new technique based on the fundamental principles of the finite element method was developed that allows the ET models to undergo the large displacements that failed in earlier simulations. Based on the idea of using less elements with higher order basis functions allows for larger

displacements in the complex 3D geometry that is present in the ET problem. Results from this new technique are very promising. A test model created with an anatomically correct lumen opening demonstrated that the new model allowed for a 262% increase in the lumen volume without any element collapse. This will allow for all the older models to be run at the full, physiological levels to even better replicate ET function.

In the future, the goal is to develop a multi-scale model of the ET that can account for the molecular scale adhesion forces referenced in Figure 1, while implementing our new large displacement method. During inflammatory conditions, it is hypothesized that due to changes in surface tension and mucosal surface conditions, molecular scale adhesion forces dominate ET function and can completely prevent the ET from opening. Also, the FSI model is going to be used along with the model of the ME to investigate the drainage mechanism of highly viscous mucus through the ET, as well as gas exchange dynamics in the ME.

## References


1. Bondy, J., et al., *Direct expenditures related to Otitis media diagnoses: extrapolations from a pediatric medicaid cohort.* Pediatrics, 2000. **105**: p. 72.
2. Bluestone, Charles D, and Klien, Jerome O., Otitis Media in Infants and Children Third edition, W.B. Saunders Company, 2001
3. Ghadiali, Samir N, Swarts, J. Douglas, and Doyle, William J. "Effect of Tensor Veli Palatini Muscle Paralysis on Eustachian Tube Mechanics." Annals of Otology, Rhinology & Laryngology 112: 8 (2003)
4. Sando, I., *A method for the histopathological analysis of the temporal bone and Eustachian tube and its accessory structures.* Ann Otol Rhinol Laryngol, 1986. **95**: p. 267-274.
5. Ghadiali, S.N., *Finite element analysis of active Eustachian tube function.* J Appl Physiol, 2004. **97**: p. 648-654.
6. Bell, E.D. *Finite Element Analysis of Clinical Pressure Flow Wave Forms in the Eustachian Tube.* Senior Thesis, Lehigh University, 2006.
7. Warrick, A.E., *Computational Modeling and Finite Element Analysis of Eustachian Tube Function in Healthy Cleft Palate Patients.* Masters of Science Thesis, Lehigh University, 2007.
8. Ghadiali S.N., Swarts, J.D., Federspiel, W.J., *Model-based Evaluation of Eustachain Tube Mechanical Properties Using Continous pressure-Flow Rate Data.* Annals of Biomedical Engineering, 2002. 30, p.1064-1076
9. Ghadiali SN, et al., *Measurement of the viscoelastic compliance of the eustachian tube using a modified forced-response test.* Auris Nasus Larynx, 2002. **29**:p. 1-5.
10. Zahnert, T., *Experimental investigations of the use of cartilage in tympanic membrane reconstruction.* Am J Otol, 2000. **21**: p. 322-328.
11. Hung, C.T., et al., *A paradigm for functional tissue engineering of articular cartilage via applied physiologic deformational loading.* Ann Biomed Eng, 2004. **32**: p. 35-49.
12. Krouskop, T.A., et al., *Elastic moduli of breast and prostate tissues under compression.* Ultrason Imaging, 1998. **20**: p. 260-327.
13. Takahashi H, Honjo I, and F. A., *Eustachian tube compliance in cleft palate--a preliminary study.* Laryngoscope, 1994. **104**: p. 83-86.
14. Gray, H., *Anatomy of the Human Body*, ed. W.H. Lewis. 2000, New York, NY: Bertleby.
15. Raadsheer, M.C., et al., *Contribution of Jaw Muscle Size and Craniofacial Morphology to Human Bite Force Magnitude.* J Dent Res, 1999. **78**: p. 31-42.
16. ADINA, *Automatic Dynamic Incremental Nonlinear Analysis Theory and Modeling Guide Volume I: Adina.* 2003, Waterford, MA: ADINA R & D.
17. Bathe, K.J., *Finite Element Procedures* 1996, New Jersey: Prentice-Hall.
18. Honjo I, Kumazawa T, Honda K, Shimojo S. "*Electromyographic study of patients with dysfunction of the Eustachian tube.*" Archive of Otorhinolaryngology 222(1) (1979) pp. 47-51.
19. Kavakli, A., Ogeturk, M., Yildirim, H., Karakas, S., Karlidag, T., Sarsilmaz., *Volume assessment of age-related conversion of the tympanic cavity by helical computerized tomography scanning.* Saudi Medical Journal, 25 (10): 1378-1381 Oct 2004

## Vita

Francis Sheer was born May 20, 1984 in McAdoo, Pennsylvania to her parents Steve and Teresa Sheer. Francis attended Marian Catholic High school where he graduated in 2002. He received his Bachelor's Degree in Mechanical Engineering from Lehigh University in 2006. As an undergraduate, Francis was a member of the Pi Tau Sigma (Mechanical Engineering Honor Society) and the Society of Automotive (SAE) Formula Team for four years. Francis then went on to get his Masters of Science Degree from Lehigh University in 2008. As a graduate student, Francis was awarded a Mechanical Engineering and Mechanics Departmental fellowship for one semester, acted as a Teaching Assistant for the Mechanical Engineering and Mechanics Department for one semester, and as a Research Assistant under his advisor, Dr. Samir Ghadiali, for one year. Francis will continue working with Dr. Samir Ghadiali at The Ohio State University for his PhD in mechanical engineering.

**Accepted Abstracts**

- Sheer, F.J., Ghadiali, S.N., "Fully Coupled Fluid-Structure Interaction Model of Active Eustachian Tube Function." In: 2008 Summer Bioengineering Conference, Poster Presentation (Marco Island, FL).

# END OF TITLE